Systematic Studies of Positron Accumulation and Transfer

![Swansea University Prifysgol Abertawe logo]

Georgia Booton

Submitted to Swansea University in fulfilment of the requirements for the Degree of Master of Science

Physics Department
Swansea University
Wales
2023

Declarations

This work has not previously been accepted in substance for any degree and is not being concurrently submitted in candidature for any degree.

Signed Gbooton...

Date 04/03/2024...

This thesis is the result of my own investigations, except where otherwise stated. Other sources are acknowledged by footnotes giving explicit references.   A bibliography is appended.

Signed Gbooton...

Date 04/03/2024...

I hereby give consent for my thesis, if accepted, to be available for electronic sharing

Signed Gbooton...

Date 04/03/2024...

The University's ethical procedures have been followed and, where appropriate, that ethical approval has been granted.

Signed Gbooton...

Date 04/03/2024...

Abstract

The Swansea positron beam line is a system comprised of a two-pressure-stage nitrogen buffer gas accumulator followed by a third stage trap. This study investigates the ballistic transfer of positrons from the two-stage accumulator to the third stage trap, with the interest to improve the understanding and efficiency of so-called "stacking" technique. The re-trapping efficiency for a single transfer has been categorised by systematically investigating parameters describing the ejected cloud, such as its parallel and transverse energy within the re-trapping region, and its subsequent behaviour within the trap, such as expansion rate and lifetime. A greater than ninety percent transfer efficiency is possible for positrons ejected from the accumulator with a 2.7 eV parallel energy spread, and positron lifetimes in the third stage trap are seen to be greater than 43 s with trap aligned on axis injection of particles and decreases with further off axis transfer injections. A variety of particle manipulation techniques (such as the magnetron manipulation) have been used to systematically study the transfer efficiencies of multiple clouds and the dynamics of these stacked clouds within the trap.

Contents

List of Figures

7

List of Tables

Acknowledgements

I wish to thank my supervisor, Professor Dirk van der Werf. Dirk has always been available to help in the lab or to answer my many questions, for which I could not be more grateful: I have had so much fun this year learning from him. Also, much appreciation is given to Dr Chis Baker for my first induction to the positron lab, many zoom calls during his busy schedule and organisation of the group meetings that were so important in realising the goals of this project. Chris also gave me an induction to SIMION program for which I am most grateful. Equal thanks are also due to Dr Aled Isaac for his expertise in positron physics and the system. Aled was always available to help in the lab, no matter how small the issue. The whole positron physics group at Swansea has been so supportive and the best introduction to postgraduate research I could have asked for. I am thankful to my CERN summer internship prior to this degree and the ALPHA collaboration who sparked my interest in antihydrogen, positrons and modern-day experimental physics. I also have my family to thank, especially my mum and dad, who have always believed in me and allowed me to follow my dreams.

Chapter 1

Introduction

1.1 History of the Positron Discovery

One of the great successes in twentieth century physics was the postulated existence of the so called 'anti-electron'. In 1928, British physicist Paul Dirac developed a theory to describe an electron moving at relativistic speeds, combining quantum theory and special relativity. There were physical interpretations to the positive and negative energy solutions of the relativistically invariant wave equation, albeit unknown to Dirac at that time [1]. Dirac then wrote a follow up paper in 1929, where he investigated the idea that the negative energy solution for the electron could be a proton, although he did acknowledge that the proton had a greater mass. The idea that the negative energy solution could be the proton was disputed by Oppenheimer in 1930 [2]. In 1931 Dirac published a paper [3], mathematically predicting the existence of the positron or 'anti-electron' from his theory, where the particle would have the same mass as the electron and opposing charge. Even though there had still been no experimental evidence thus far, he expressed his surprise to "if nature had made no use of it". Dirac shared the Nobel prize with Schrödinger in 1933. Unaware of Dirac's equation, Carl Anderson experimentally observed the positron in the fall of 1932. He presented a paper [4] with photographs of cosmic ray tracks, for which he shared the Nobel Prize in Physics in 1936 with Walter Hess. Occhialini and Blacket who worked in Cambridge, confirmed the discovery of positrons in February of 1933, by studying photos taken with the Cavendish Cloud chamber. Occhialini and Blacket related their findings to Dirac's quantum theory.

In 1934, Curie and Joliot published an article describing the production of a new kind of radio-element. They observed positron emission from boron, magnesium or aluminium long after they had stopped bombarding the target with alpha particles. From this, they were able to calculate the half life period of activity [5]. This was the first production of artificially produced radioactive atoms. It can be said that this discovery changed the course of physics, and as a result, opened up large areas in radioisotope research and applications in medicine: they received

10
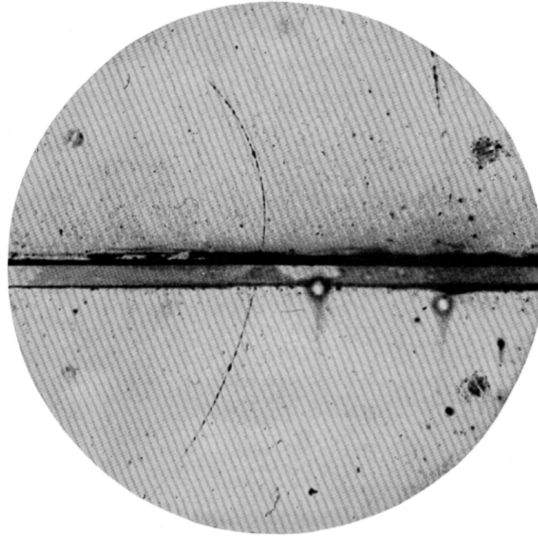
Figure 1.1: Extracted from [4]. Cosmic ray tracks presented by Anderson in 1932, captioned as "A 63 million volt positron passing through a 6mm lead plate and emerging as a 23 million volt positron. The length of this latter path is at least ten times greater than the possible length of a proton path of this curvature".

the Nobel prize in in chemistry in 1935.

The positron was found to have a specific and unique use in medicine. In 1973, the first Positron Emission Tomography (PET) scanner was built. PET is a functional medical imaging technique in which the properties of positron annihilation are utilised to image the body. A radio-pharmaceutical is synthesised from a positron emitting nuclide, one example is fluordeoxyglucose, where radioactive F^{18} is chemically bonded to a targeting agent, which may have a specific biomedical function. The radio-pharmaceutical is injected into the patient where is travels through the bloodstream. Fluorodeoxyglucose is used to image cancerous tissue, and cancerous cells have a greater metabolic activity than non-cancerous cells therefore the injected radio-pharmaceutical is more concentrated in those cancerous tissues. The positrons are therefore emitted in those cancerous cells and can travel distances up to 1mm before reaching thermal energies and annihilating with an electron. The gamma photons produced from annihilation are detected and the source localized to then reconstruct a 3-dimensional image of the patient. The functional properties of PET imagining make the technique particularly useful in cancer diagnosis and treatments.

1.2 Research Interests

The study of antimatter in general is an exciting field. The CPT theorem states that the laws of physics are invariant under the combined actions of charge conjugation (C), parity (P) and time reversal (T). The positron has the same mass,

magnitude of electric charge, and gyromagnetic ratio to the electron, only where the sign of the electric charge is positive. There are no known exceptions to the CPT theorem. Many experiments worldwide are researching to find any slight exceptions yet there are still many unanswered questions to why there is an abundance of matter over antimatter and hence why does the universe exist.

Most experiments that require positrons need the particles readily available in large numbers, often in intense bursts of desired energy spread and pulse length. The development of the buffer gas trap by surko and co-workers [6, 7] enabled large numbers of positrons to be accumulated and ejected in a burst. Buffer gas traps are used in many experimental groups around the world, especially at CERN where many collaborations work towards antihydrogen research, such as ALPHA [8], GBAR [9], ASACUSA [10], AEgIS [11] and ATRAP [12].

However, the buffer gas trap has limitations. The particle lifetime is relatively short due to the gas pressure, therefore there is a need for a transfer process to subsequent traps with more desirable conditions. The transfer regards to the movement of particles from where they are produced to a different part of the experimental setup, and the efficiency in which this process is completed is deemed the transfer efficiency. The so called 'stacking' technique has become of relevant interests due to the ability to store even larger amounts of particles that are ejected from a trap such as a buffer gas trap. Once stacked, positrons on the order of millions can be trapped and are then readily available for experimental study such as antihydrogen synthesis or positronium spectroscopy studies. The ATHENA collaboration used the stacking technique of positron plasma under UHV conditions between two solenoids and achieved an overall transfer efficiency of 34% in 2003 [13]. Recent developments have seen a vast increase in the transfer efficiency. The GBAR collaboration have shown that their transfer efficiency to dependant on the well depth, and after accumulating 10 stacks in the accumulator, their transfer efficiency is 80% [9].

1.3   Thesis Outline

The second chapter introduces some theoretical concepts surrounding positron trapping, such as the production of positrons, and charged particle traps. The third chapter describes the Swansea positron beamline, with an explanation of the hardware such as the accumulator assembly, the vacuum and gas system, and experimental control. The basic principles of positron accumulation are detailed through accumulation curves obtained and some operational procedures. The variation of gas pressure in the two-stage accumulator is shown here and yields information regarding the accumulator and its operational state.

The fourth chapter details positron transfer. The two-stage accumulation procedure was optimised with a view for transfer and stacking. Some experiments were taken to characterize the cloud accumulated in the two-stage accumulator

in the form of parallel energy measurements with and without the use of a high voltage pulse generator, alongside simulation. A transfer efficiency was obtained for the successful re-trap of a single positron cloud. The fifth chapter details a technique used to overcome trap misalignment through the use of magnetron orbit excitation to align the cloud on axis to the center of the third stage trap. The expansion rate and lifetime of particles are taken at different radial injection positions. The sixth chapter then begins to examine the re-trapped cloud in the third stage, through the use of parallel energy measurements, efficiencies and particle losses. The dynamics between two clouds trapped in the third stage is experimentally investigated, and then multiple clouds are stacked in the third stage. The final chapter summarises the conclusions drawn form the experiments performed and suggests the application of this work, and future work, to be carried out.

Chapter 2

Background Theory

2.1 Positron Sources and Production of Slow Positron Beams

The sources of positrons in nature are radioactive beta decay or pair production. During pair production, a photon is converted into an electron and a positron via $\gamma + X \rightarrow e^+ + e^- + X^*$. The particle X must be present to conserve momentum and the photon must have an initial energy greater than that of the sum of the rest masses of the electron and positron. The GBAR collaboration at CERN generate positrons with a linear accelerator (LINAC) [14]. Electrons are accelerated up to 9 MeV and hit a tungsten target and produce large numbers of positrons by pair production. Advantages for using a LINAC based method is a greater beam intensity and no persistent radioactivity, however broad beam energy spreads and pulse widths can be seen that are not desirable for trapping [15]. When using a radioactive source, a proton or neutron rich nuclei decays to produce a beta plus or beta minus particle (positron or electron). In the case of positron production, a proton decays into a neutron producing a positron and an electron neutrino; $^A_Z X \rightarrow\, ^A_{Z-1} X + e^+ + \nu_e$.
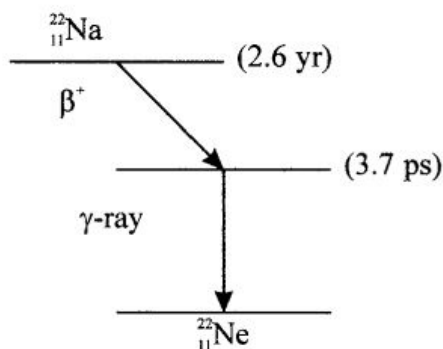
Figure 2.1: Simplified decay channel for ^{22}Na. Figure extracted from [1].

Sodium 22 is often used as a beta source material due to its relatively long half life of 2.6 years in comparison to other β^+ emitters, convenient for beam line applications. The positron branching ratio of ^{22}Na is around 90 %, where the positron emission is promptly followed by a gamma ray of energy 1.274 MeV. The remaining 10 % of the branching ratio is electron capture. The simplified decay channel is shown in figure 2.1.

2.2   Moderation

The positron beam emitted initially has a larger than desired energy spread on the order of keV for the intention of trapping, therefore the positrons need to be 'cooled down'. Moderation is the process of producing positrons with a narrow energy spread with energies of 1-2 eV [1], as shown in figure 2.2. As positrons enter the moderator with often high energies, they loose large quantities of kinetic energy via inelastic collisions through electronic ionization and excitation [16]. Many positrons are lost through annihilation, but a very small percentage are not lost, and are left with kinetic energies a few eV. At lower energies, the loss mechanisms are highly dependant on the type of material. Early moderators used materials where the surface had a negative work function. When the positrons reach thermal energies, they diffuse through the material to the surface where the negative work function may cause a positron to be emitted. Tungsten was first reported to have an efficiency of $(3.2 \pm 0.4) \times 10^{-3}$ [17], and is now the most commonly used metal moderator. Some materials with a positive work function show positron emission, such as rare gas solids (RGS). Once the positron energies are low, they can only loose energy by creating low energy phonons. The large diffusion length in such materials means the positron can reach the surface with sufficient energy to overcome the work function [18]. Neon has an efficiency of 1 %, which is the most efficient [19].

2.3   Trapping Charged Particles

To successfully trap any type of particles, confinement is all direction of motion is needed. The principles of the Penning trap were first noted by Penning in 1936 [21], although not originally forseen as a charged particle trap. The first Penning trap was built by Dehmelt, who took the inspiration from the Penning ion gauge. In its simplest form, a Penning trap is formed from two grounded end caps and an electrically biased ring electrode. Dehmelt was able to trap electrons for 10 s [22, 23]. The penning trap was modified and improved upon by Malmberg to produce the Penning-Malmberg traps that are used today for charged particle trapping.
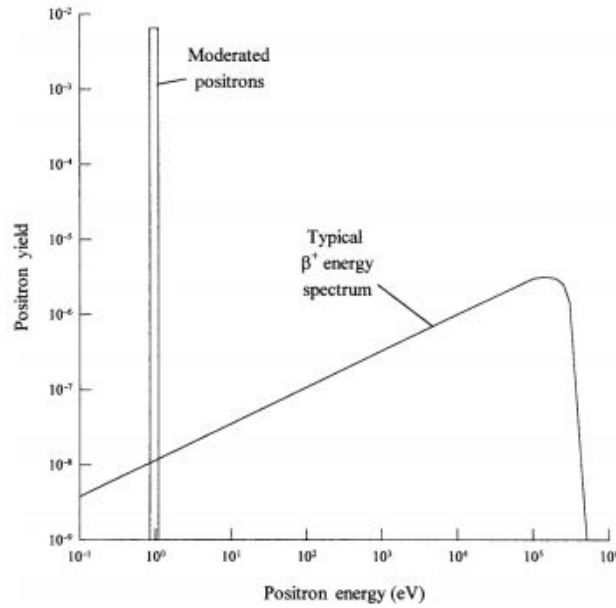
Figure 2.2: β^+ spectrum of particles before and after moderation. Figure originally presented in [20].

2.3.1 Penning Trap

A charged particle moving through an electric and magnetic field experiences a Lorentz force given by

$$\boldsymbol{F} = q(\boldsymbol{E} + \boldsymbol{v} \times \boldsymbol{B}). \tag{2.1}$$

If only a magnetic field is present, the particle will move with a so called free cyclotron motion, with a constant velocity along the axis of the applied magnetic field. The free cyclotron motion is given by

$$\Omega_c = \frac{q\,|B|}{m}. \tag{2.2}$$

However, in the presence of an electrostatic potential, given by

$$\phi(x, y, z) = \frac{V_0}{2d^2}(z^2 - \frac{x^2}{2} - \frac{y^2}{2}), \tag{2.3}$$

where the d is a constant related to the trap geometry given as,

$$d^2 = \frac{r_0^2}{2} + z_0^2, \tag{2.4}$$

the equation of motion is

$$m\ddot{\boldsymbol{r}} = q(-\boldsymbol{\nabla}\phi + \dot{\boldsymbol{r}} \times \boldsymbol{B}), \tag{2.5}$$

where $\boldsymbol{r} = (x,y,z)$. The differential equations derived from the equation of motion are

$$\ddot{x} = \frac{q}{m}\left(\frac{V_0 x}{2d^2} + \dot{y}B_z\right) \tag{2.6a}$$

$$\ddot{y} = \frac{q}{m}\left(\frac{V_0 y}{2d^2} - \dot{x}B_z\right) \tag{2.6b}$$

$$\ddot{z} = \frac{-qV_0}{md^2}z. \tag{2.6c}$$

From the equation in the 2.6c it is seen that the axial bounce frequency is given by,

$$\omega_z^2 = \frac{V_0 q}{md^2}. \tag{2.7}$$

With a magnetic field of 50 mT, the cyclotron motion angular frequency is approximately 8.8 GHz. Equations 2.6a and 2.6b are coupled, and can be solved using a substitution such as $U = x + iy$. The equations then become

$$\ddot{U} = \frac{\omega_z^2}{2}U - i\Omega_c \dot{U}, \tag{2.8}$$

which can be solved with an ansatz $U = e^{-i\omega t}$, giving,

$$2\omega^2 - 2\Omega_c\omega + \omega_z^2 = 0, \tag{2.9}$$

where the roots are found to be

$$\omega_\pm = \frac{\Omega_c}{2} \pm \sqrt{\Omega_c^2 - 2\omega_z^2}. \tag{2.10}$$

The positive root describes the modified cyclotron frequency (ω_c), whereas the negative root describes the magnetron motion (ω_m). Typically, the motion frequencies have a hierarchy such as $\omega_c > \omega_z > \omega_m$, otherwise particles cannot become trapped. The result motion of trapped particles is a combination of three harmonic oscillatory motion; small cyclotron oscillations, axial bounce motion, and a larger magnetron motion, which are visualised in figure 2.3.

2.3.2 Penning-Malmberg Trap

The Penning-Malmberg trap is a variation of the Penning trap, and uses a combination of electrostatic and magnetic fields for confinement. A Penning trap produces perfectly quadratic electric potentials due to the geometry of the hyperbolic electrodes that provide stability in three dimensions. The electrodes in a Penning-Malmberg trap are hollow cylindrical electrodes, where the geometry is preferable due to the open 'end cap', thus allowing transfer and ejection of particles into subsequent traps or destructive detection.
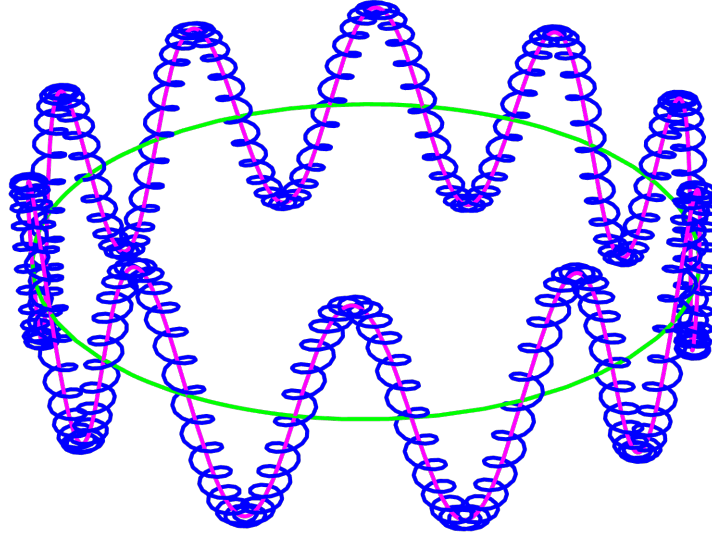
Figure 2.3: The three oscillatory motions of a charged particle in a Penning-Malberg trap, the cyclotron motion (blue), axial bounce motion (pink) and the magnetron motion (green).

2.3.3   Buffer Gas Traps

The buffer gas trap (BGT) was invented by Surko and co-workers [6, 7]. The original design of the trap consists of a modified Penning-Malmberg trap that used cylindrical electrodes with 3 distinct stages of increasing internal diameter, thus creating 3 separate pressure regions, shown in figure 2.4. The axial confinement is given by an electrostatic potential, and the radial confinement provided by a solenoid enclosing the electrodes. The principle is that positrons enter the buffer gas accumulator after moderation, and quickly loose kinetic energy upon interaction with the buffer gas. The positrons are trapped in successively deeper wells, where the heights are tuned to maximise the trapping efficiency, as they loose energy and cool down. The lifetime of particles is maximum when trapped in the lowest pressure region. Molecular nitrogen is the buffer gas of choice because its electronic energy level is below that of positron formation, the dominant loss mechanism. Figure 2.4 shows the gas inlet in stage 1 of the accumulator, and how the pressure decreases in the stages where the electrode inner diameter is increased. The lifetime of particles in a trap such as this one is of the order of 100 s. The loss mechanism is annihilations on the background gas.
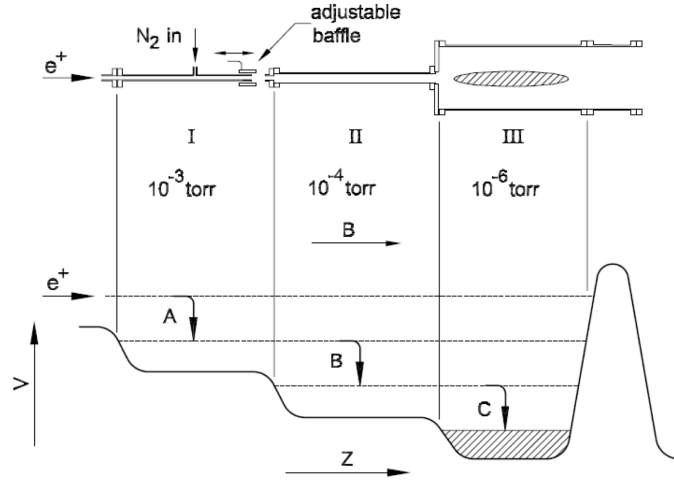
Figure 2.4: The buffer gas trap originally designed and presented by Surko and co-workers in reference [24] with three distinct trapping and pressure regions that facilitate a 9 eV loss per stage A, B and C (see section below).

2.4   Energy Loss Mechanisms

The positrons are decelerated and loose energy upon an interaction with a gas molecule in the following processes; elastic scattering, rotational and vibrations excitation, electronic excitation, and direct ionisation. Molecular nitrogen has been shown to have the greatest trapping efficiency, due to its electronic excitation threshold, published by Surko and Greaves [24]. The most predominant loss mechanism for incoming positrons is electronic excitation, with an energy loss of around 9-11 eV per collision [6], dependant on the energy thresholds (see table 2.1). However, when a positron undergoes an inelastic collision with a

Table 2.1: Positron interactions with nitrogen

Mechanism	Interaction	Energy Required
Annihilation	$e^+ + N_2 \rightarrow N_2^+ + 2\gamma$	All
Elastic Scattering	$e^+ + N_2 \rightarrow e^+ + N_2$	All
Vibrational excitation	$e^+ + N_2 \rightarrow e^+ + N_2$	0.3 eV
Rotational excitation	$e^+ + N_2 \rightarrow e^+ + N_2$	0.001 eV
Electronic excitation	$e^+ + N_2 \rightarrow e^+ + N_2^*$	>8.6 eV
Positronium formation	$e^+ + N_2 \rightarrow Ps + N_2^+$	>8.8 eV
Ionization	$e^+ + N_2 \rightarrow N_2^+ + e^+ + e^-$	>15.6 eV

molecule, they can be radially transported to the walls of the electrode, where they annihilate [25]. This action is overcome by the introduction of the rotating dipole electric field (also called a rotating wall - see below).

2.5   Rotating Walls

The term 'rotating wall' (RW) is the name given to a special electrode which is radially segmented and has an applied phase-shifted and time-varying sinusoidal voltage to each segment. The rotating wall technique has been previously shown to be successful in the plasma regime and in the single particle regime [26]. The rotating wall compresses the positron cloud (also known as axialisation) and therefore reduces annihilation on the edges of the trap electrodes. The driving of the particles also causes heating, which can be overcome with the addition of a cooling gas. Sulfur hexafluoride has previously been shown to be the best cooling gas by Surko and Greaves [24]. Sulfur hexafluoride has the shortest cooling time when tested against other cooling gases such as CF_4 and CO_2, as shown in table 2.2

Table 2.2: Positron annihilation (τ_a) and cooling (τ_c) times, data from [24].

Gas	τ_a (s)	τ_c (s)
SF_6	2190	0.36
CF_4	3500	1.2
CO_2	3500	1.3
N_2	6300	115

2.6   Single Particle and Plasma Regimes

Particles that are defined in the so called 'single particle regime' have orbital and axial motions defined by the magnitude of the trapping potentials [27], and a collection of particles defined by the single particle regime are called clouds. The inter-particle interactions can be ignored in the single particle regime. Under certain circumstances, enough particles can be accumulated to create a positron plasma. A plasma is a state of matter where self generated electric fields affect the forces which the particles in the plasma experience. A plasma is characterised by the Debye screening length, which is the distance that particles shield external fields. The Debye screening length λ_D is given as

$$\lambda_D = \left(\frac{k_B T \epsilon_0}{n_e e^2} \right)^{\frac{1}{2}}, \tag{2.11}$$

where k_B is the Boltzmann constant, T is the temperature of particles, n_e is the density of particles, ϵ_0 is the permittivity of free space and e is the charge of the electron (or positron with opposite sign). To qualify as a plasma, λ_D must be smaller than any of the dimensions of the positron cloud. The Swansea positron beamline can be capable of producing plasmas with a highly optimised system, however in the case of this study, experiments are operated mostly within the single particle regime unless otherwise stated.

Chapter 3

Apparatus and Experimental Methods

This chapter describes the layout of the Swansea beam line and key features. Basic operational procedures are also detailed here.

3.1 System Overview
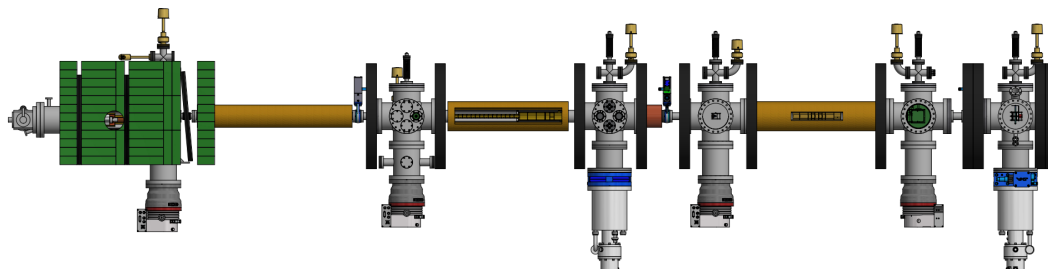
Figure 3.1: Schematic of the current Swansea positron beam line, comprising the source chamber (left) with the lead housing visible, buffer gas accumulator (middle), storage trap (middle right), and laser/target/sample cross (right).

Figure 3.1 shows the elements that comprise the Swansea positron system in its current state. Further technical details which are not discussed in this section can be found elsewhere [28].

3.1.1 The Positron Source and Moderator

Positrons are emitted from a 2100 MBq radioactive ^{22}Na source (activity measured on installation 28/03/2018). The positrons undergo moderation from a neon rare gas solid (RGS) moderator. Over time the efficiency of the moderator decreases as the moderator decays, and therefore has to be 'regrown' periodically after a number of weeks. The process is visualised in figure 3.2 where the pressure and temperature of the source chamber is measured, as well as the counts during

moderator growth. The source is warmed to around 30 K or greater, allowing the condensed neon to evaporate. The source is then cooled back down to around 6-7 K and then the pressure increases to 2×10^{-3} mbar as the neon is admitted to the source chamber. The pressure is kept stable by a piezoelectric valve controlled by a proportional integral derivative (PID) loop control. The neon is left to condense onto the source assembly for approximately 30-50 minutes. The count rate is the number of positron annihilations per second and is measured by a Cesium Iodide detector via positron annihilations on the closed valve at the beginning of the beamline (before the first guiding coil). The admittance of the neon gas is stopped when the count rate reaches a plateau, and the physical values that allow the gas into the source chamber closed, leaving a layer of solid neon on the source assembly. The count rate during moderation is suppressed during the growth due to scattering and annihilation on the uncondensed neon gas in the source chamber, and a sudden jump is seen once the gas has been removed and returned to a base pressure. A mean and a standard error of the count rate is taken after the process of growing a new moderator with a subtraction of the background count rate.

Figure 3.2: LabVIEW front panel for moderator growth. The temperature and pressure of the source chamber, and the counts are measured throughout and displayed.

3.1.2 Vacuum and Gas System Control

The system is kept under vacuum. Outlined in figures 3.3 are the two different types of vacuum pumps used; cryogenic and turbo. The turbo pumps are backed by scroll pumps not shown in the figure. The vacuum specifications are shown in the table 3.1.
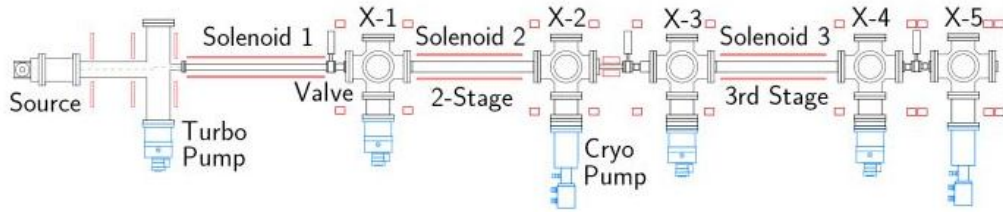
Figure 3.3: Schematic of the system showing the vacuum system (black), high vacuum pumps (blue), and solenoids. The MCP detector is at the right side of X-5, along with a CsI detector sat on top of X-5. There is also a second CsI detector that can be moved, but is normally placed at X-3 for the duration of this study.

Table 3.1: Vacuum Specifications

Position	Pump Type	Base Pressure
Source	Turbo	10^{-9}
X1	Turbo	10^{-8}
X2	Cryo	10^{-8}
X3	Turbo	10^{-8}
X4	Turbo	10^{-7}
X5	Cryo	10^{-7}

There are also three different types of pressure gauges to measure the pressures along the system; Pirani, capacitance and Penning cold cathode. The pressure reading from the penning gauges is dependent on the type of gas and therefore need a calibration factor to measure different gas pressures. High purity molecular nitrogen is used as the buffer gas N_2 and there is a cooling gas (currently SF_6), with Ne gas for moderator growth. Each is regulated into the system by a piezoelectric valve that controls the flow of gas. The pressures are monitored by a PID loop controller to ensure the pressures are kept stable.

3.1.3   Experimental Control

The sequencer manages the timing control, analogue and digital inputs and outputs integrated into a software. A full and detailed explanation of the hardware and software for experimental control can be found elsewhere [16, 27, 29]. There are 16 analogue outputs available that each have a range of ±10V, with a minimum step of 3μs. The analogue outputs are used with an amplifier therefore voltages of ±140V can be achieved. There are also a range of digital outputs available to use, which have a minimum step time of 12.5ns. The digital outputs are used to trigger equipment such as fast pulse generators or rotating wall function generators. LabVIEW software allow sequences to be created, modified and grouped easily. Screenshots are shown in figure 3.4 of the editor.
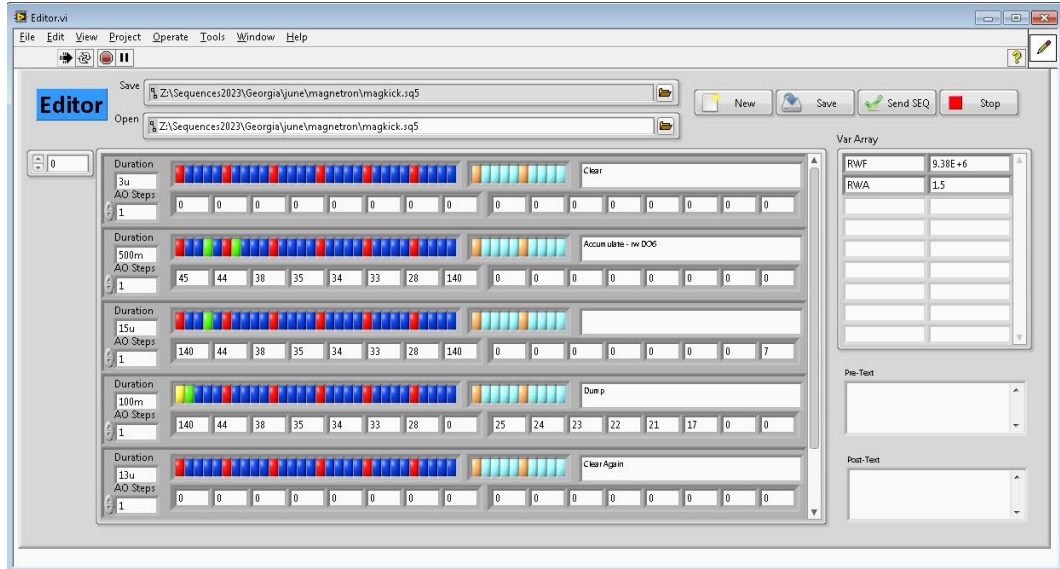
Figure 3.4: Screenshot of the sequence editor software

The sequence is composed of lines, each with its own time step duration. The analogue outputs are given by the 16 white boxes populated with a voltage that is requested to be applied to the electrode. The coloured tabs represent the digital outputs, which command an outcome depending on the way the digital outputs are connected. To the right of figure 3.4 there is a 'Var array' which populates information for the rotating wall. The frequency given by RWF and the amplitude given by RWA. These parameters are sent to another LabVIEW software once requested.

3.1.4 Magnetic Fields

Particles are radially confined by multiple coils and solenoids placed along the beam line. The system currently has three different types of magnets, so called 'pancake coils', steering coils and solenoids, and their approximate magnetic field strengths can all be calculated using Ampere's law. The solenoids provide the magnetic field necessary for radial confinement in the buffer gas trap. The magnetic field given by the solenoid is approximately constant, and is given by,

$$|B| = I N \mu_0 \frac{N_L}{L}, \tag{3.1}$$

where I is the current through the solenoid, L , N_L and N are the length, total number of turns per layer and number of layers on the solenoid respectively. The first solenoid (refer back to figure 3.3) has a length of 890 mm, $N_L = 4$, $N = 220$ giving a field strength of 1.24 mT A^{-1}. With a current of 25 A, the magnetic field strength is approximately 30 mT. Solenoid 2 and 3 are identical, and both give a magnetic field strength of 1.257 mT A^{-1}. The solenoids normally have a current of 30 A, so the magnetic field strength is approximately 40 mT.

The pancake coils give a magnetic field strength in the center of around 30 mT, approximated by,

$$|B| = I\Sigma_{m=0}^{N} \frac{\mu_0}{2(r_o + mr_1)},$$
(3.2)

where I is the current through the pancake coil, r_0 is the inner radius of the coil, r_1 is the thickness of each layer and N is the number of layers in the stack. The pancake coils are two coils placed together, and give a magnetic field strength at the center of 0.722 mT A^{-1}. The pancake coils have a current of 15 A, therefore the magnetic field at the center is 10.83 mT. The steering coils are to provide a field along the beamline, and are in an approximate Helmholtz configuration. They have an approximate field strength in the centre given by,

$$|B| = IN \frac{\mu_0}{r_{in} + r_{out}},$$
(3.3)

where $r_{in,out}$ is the inner and outer radius of the steering coil respectively. The field provided is 0.900 mT A^{-1}, and are each energised with approximately 6.0 A, with slight variations to steer the beam. This results in a magnetic field strength of 5.4 mT.

3.2 Detection

3.2.1 CsI Detectors

Two Caesium Iodide (CsI) detectors have been installed to detect the gamma photons emitted during annihilation. The detectors have an output that is proportional to the number of positrons. A CsI detector is a scintillation based detector. The gamma rays that are emitted from positron annihilation hit a luminescent material where the energy is absorbed. These crystals have a large light output and an emission spectrum well suited to coupling with silicon photodiodes. The signal outputted from the detectors is digitised and read from a LabVIEW program. The signal resembles that in figure 3.5.

3.2.2 Micro-Channel Plate

A Micro-channel plate (MCP) is a diagnostic used to image charged particle clouds or plasmas in combination with a phosphor screen. An MCP is an electron multiplier, and consists of millions of glass lead channels in the arrangement of a chevron, shown in figure 3.6. The surface of the glass channels provides a semiconducting layer from the coating of a metal. Charged particles hit the surface of the MCP front, and emit electrons. Those electrons are then accelerated to the MCP back, due to the electric field, and subsequently more electrons are released. At the bottom, electrons are accelerated to a phosphor screen, where light is emitted due to the collisions on the screen. The front of the MCP will have a positive or negative voltage applied dependent on the charge of the particles
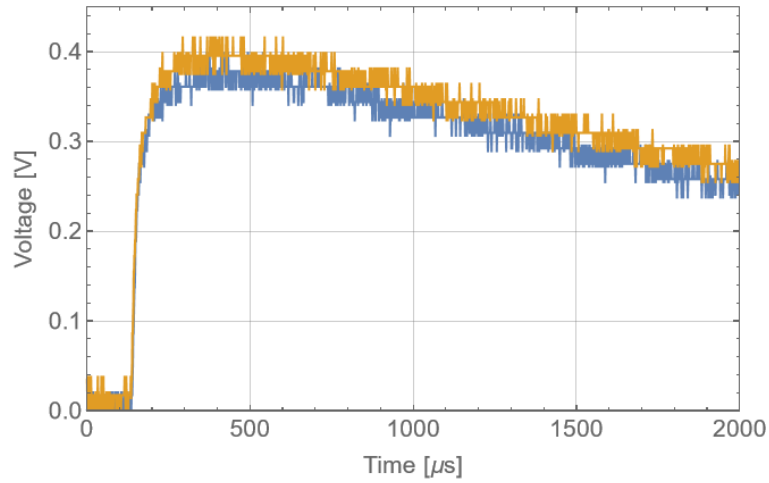
Figure 3.5: Signal from the CsI detector. In this example, there are 2 repeats of the same measurement. A data point is formed by taking a mean measurement of the mean peak voltage minus the mean background signal. A standard error is calculated from repeat measurements.
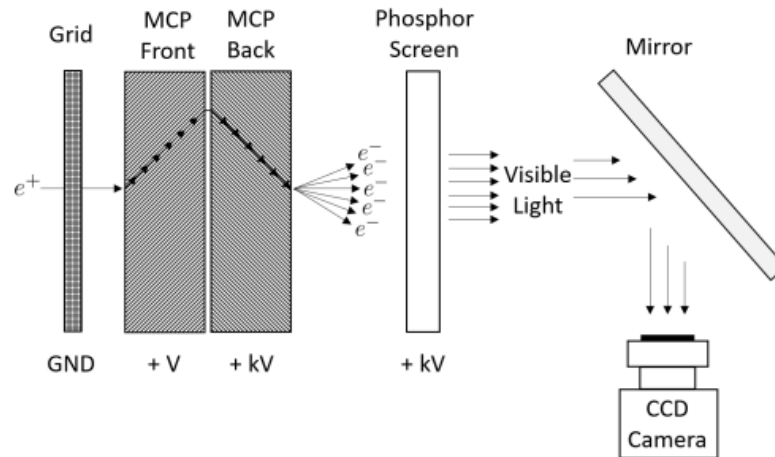
Figure 3.6: Figure extracted from [30]. The MCP setup for positron detection, showing the grounded grid, MCP front, back and phosphor screen and mirror.The CCD camera sits outside the vacuum and images through a view port.

in the beam line. Typical voltages on the front plate are -100 V, back plate at 2.2 kV, and the phosphor screen set at 4.6 kV. The 2D optical image produced is reflected by a mirror set at 45 degrees so that the image is captured by a CCD 12 bit camera that sits outside the vacuum system. The integrated data can be

fitted by a one dimensional Guassian,

$$G(x) = A \exp\left(-\frac{(x - x_0)^2}{2\sigma^2} \right) + B, \tag{3.4}$$

where x_0 is the center of the cloud in Cartesian coordinates and A, σ and B are fitting parameters. The processed image and integrated intensity is shown in figure 3.7. Data can be extracted about the central density, size, and position of the cloud.

a)   b)
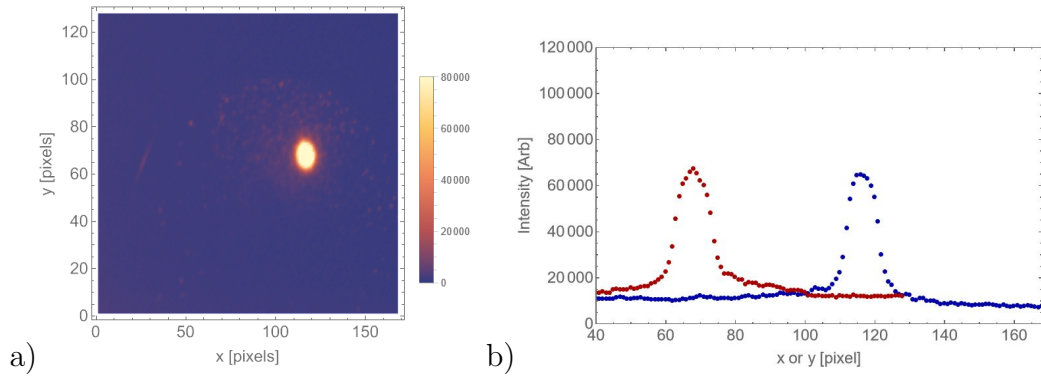
Figure 3.7: a) Intensity plot produced from MCP data in Mathematica, with the colour bar representing the relative intensity. b) Integrated intensity plot with two 1D Gaussian fits across x and y pixels.

3.3 The Accumulator

The accumulator, as shown in figures 3.1 and 3.3 consists of a two stage buffer gas trap followed by a third stage trap (sometimes referred to as a storage trap). Each stage has a different electrode structure, as detailed below.

3.3.1 Two Stage Assembly

The two stage accumulator consists of two cylindrical penning traps of different diameter as shown in figure 3.8. The first stage has 15 electrodes with an inner diameter 10 mm and length 24 mm. The second stage has 5 electrodes of larger inner diameter 41 mm and length 50 mm. The increase in diameter facilitates the decrease in pressure. The electrodes are kept electrically isolated from each other by the use of 2 mm diameter sapphire balls. The electrical connections are also shown in 3.8; E0, 'Grad high' and 'Grad low' are connections to the first stage that give each electrode an independent electrostatic potential, where the 14 electrodes each have a potential in a slowly decreasing gradient between the voltage requested at 'grad high' and 'grad low'. The connections for the second stage are E1-E5. One half of the E4 electrode is segmented to give rotating dipolar

electric field (Rotating wall). Nitrogen buffer gas is admitted to the accumulator through a small hole in the middle of the first stage.
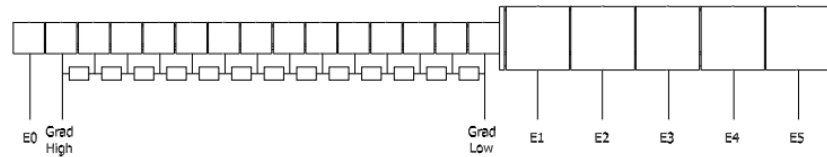
a)
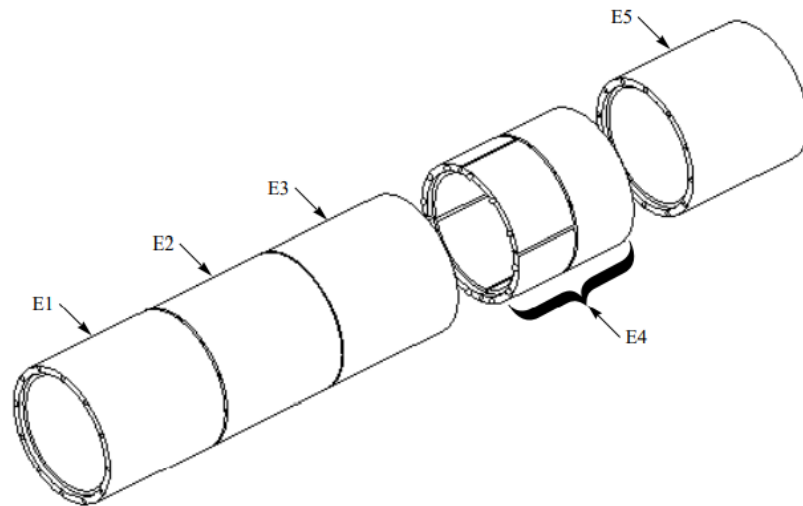
b)

Figure 3.8: AutoDesk Inventor ^{TM} design picture of the two-stage buffer gas trap electrode assembly. a) The two-stage assembly with electrode labels. The potentials applied between 'Grad High' and 'Grad Low' are supplied by a series potential divider. b) Side view of the second stage only showing the dipolar rotating wall electrode.

3.3.2 Third Stage Assembly

The pressure in the third stage independent trap is much lower, thus allowing for a much longer lifetime for various experiments. There are 9 electrodes of varying length detailed in figure 3.9, again, electrically isolated by 2 mm sapphire balls, and two rotating walls segmented into 6 electrodes each. The two rotating walls are given an applied phase shifted voltage, if desired, by a custom built function generator. However, if not desired, each segment of the electrode can be

connected in series to create a static potential across each segment. The entire axial length of the third stage is 250 mm.
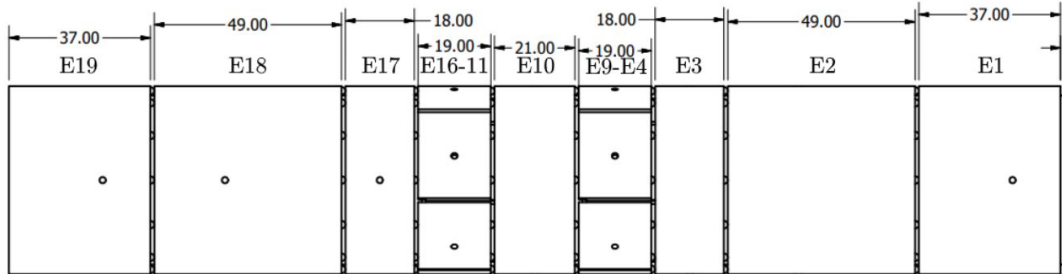
Figure 3.9: Side view AutoDesk Inventor ^{TM} design picture of the third stage electrode assembly. The electrode lengths given in mm, with the electrode labels. The internal diameter of each electrode is 41 mm. Visible are the electrode connections and sapphire spheres between each electrode. Positrons enter on the left hand side.

3.4 Basic Accumulation Experiments

Positron accumulation is governed by the equation,

$$\frac{dN(t)}{dt} = R - \frac{N(t)}{\tau}, \tag{3.5}$$

relating the number of particles in the trap, N, to a rate of accumulation, R, and a particle lifetime τ. Integrating both sides we get

$$N(t) = R\tau(1 - e^{-t/\tau}). \tag{3.6}$$

The signal from the detector, given in volts, has an output proportional to the number of accumulated positrons $N(t)$. An example of an accumulation curve performed in the two stage buffer gas trap is given in figure 3.10. At short times when $t \ll \tau$, the accumulator fills at a constant rate of accumulation. For longer times (considering $t \to \infty$), the number of positrons curves off at a saturation level $R\tau = n(\infty)$. If the accumulation is stopped with a number of particles N_0 in the trap, the number of particles in the trap after holding for a time t, is given by

$$N(t) = N_0 e^{-t/\tau}, \tag{3.7}$$

assuming a constant loss rate based upon the constant gas pressure admitted to the trap. Throughout this thesis, the positron number is reported as a direct comparison to the output of the caesium iodide detectors, that measure the annihilation signal. An exact calibration has been done previously, yet the voltage detection during this work is on the order of micro volts, which is too small to make an accurate calibration. Therefore, the CsI signal can be interpreted as proportional to the number of positrons where presented.
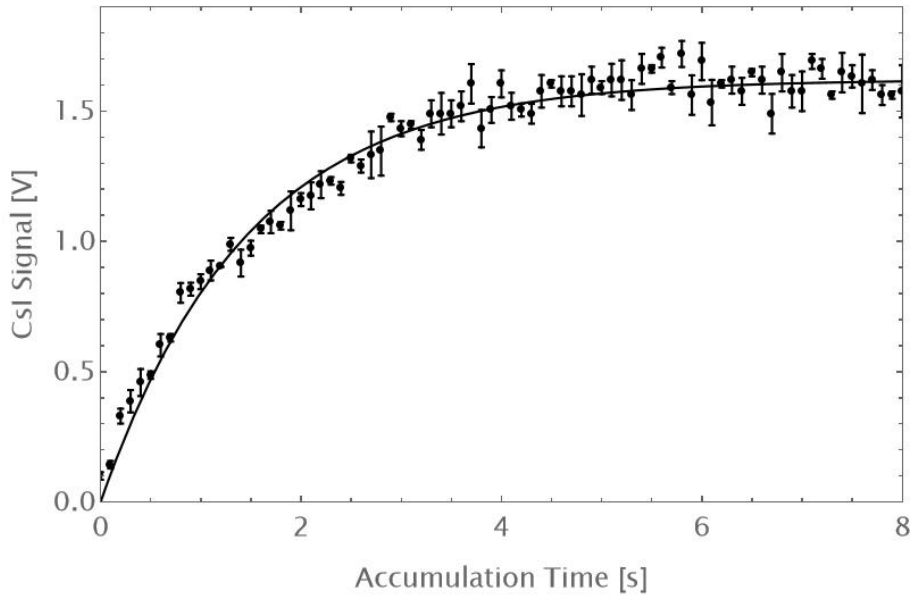
Figure 3.10: An example accumulation curve. Curve fitted with equation 3.6. The nitrogen buffer gas pressure is 1×10^{-5} mbar. Fitted parameters $R = (1.11\pm0.03)$ V/s, $\tau = (1.45\pm0.04)$ s. The rotating wall is on at a fixed frequency of 9.65 MHz and an amplitude of 2 V, with the addition of a cooling gas.

3.4.1 Pressure Dependence

Pressure dependent measurements of the accumulation rate and lifetime were performed on the Swansea accumulator and published in reference [28] in 2006. The measurements detail the behaviour of the accumulator from that expected from such an instrument. The accumulated positrons will form a cloud (depending on the density) in the first two stages of the trap. The positron trapping rate can be expressed as the product of the incoming beam intensity I_0, and the trapping efficiency ϵ, namely,

$$R = I_o\epsilon. \tag{3.8}$$

The trapping or capture efficiency ϵ is given by

$$\epsilon = f(1 - e^{-DP}), \tag{3.9}$$

where P is the buffer gas pressure, D is a constant proportional to the cross section for positron-nitrogen interactions and f is the branching ratio determined by the ratio of the cross section for the electronic excitation of the molecule in a positron-N_2 collision. The positron lifetime is expected to be inversely proportional to the buffer gas pressure as,

$$\tau = \frac{1}{\lambda} = \frac{1}{BP}, \tag{3.10}$$

where B is a constant at fixed temperature and is related to the Z_{eff} of N_2 (the effective number of electrons in the molecule available to the positron for

30

annihilation [31]). The expected behaviour for an ideal accumulator is given as,

$$n(\infty) = fI_0 \frac{(1 - e^{-DP})}{BP}. \tag{3.11}$$

This equation assumes that positrons are transferred between stage one and two with unit efficiency. There exists a modified equation of the ideal accumulator in reference [28], that postulates a pressure independent loss factor between the two stages. This introduces another branching ratio of generic form *EP / (EP + F)*, leading to the actual behaviour of the accumulator,

$$n(\infty) = \frac{fI_0 E}{B} \left(\frac{1 - e^{-DP}}{EP + F} \right), \tag{3.12}$$

where F is a constant and EP is the probability of capture in the second stage. The inverse pressure dependence at high pressures is retained, yet at low pressures $n(\infty)$ is proportional to P.

A number of accumulation curves were obtained at different nitrogen gas pressures to observe the relationships between nitrogen buffer gas pressure and R, τ and $n(\infty)$. The following measurements were all taken with no rotating wall applied. A plot of the rate of accumulation as a function of nitrogen gas pressure is given in figure 3.11, and a plot of the inverse lifetimes obtained in figure 3.12; from those plots, information regrading the system such as constants fI_0, B and D are extracted and therefore enable the plot of the ideal accumulator from equation 3.11 to be made.

Figure 3.13 shows the saturation intensity $n(\infty) = R\tau$ as a function of gas pressure. It is desirable to have $n(\infty)$ as great as possible. Figure 3.13 shows the ideal buffer gas pressure for $n(\infty)$ is estimated at around 1.65 x 10^{-5} mbar. The observed and expected behaviour of the accumulator are plotted on figure 3.13, by the solid and dashed line respectively. At higher pressures, the trend in the observed and expected behaviour are in fair agreement (and would tend to the same value if more data was taken at slightly higher pressure), yet at low pressure we observe $n(\infty)$ is proportional to P, which is not in agreement with the ideal behaviour of the accumulator, yet agrees with the modified equation describing the actual behaviour with the inclusion of the pressure independent loss factor. The pressure independent loss factor is thought to be due to trap asymmetries. A similar result can be found to equation 3.12 if the lifetime in equation 3.10 has an additional constant c as the fitted data from figure 3.12 suggests by inspection, due to additional background gas. The case where there is background gas present giving a non zero intercept on figure 3.12 was discussed in reference [28].

3.4.2 The Rotating Wall Effect

The scan over a rage of frequencies identifies the bounce frequency of particles in the two-stage trap, for a range of drive amplitudes. The resonant frequency is
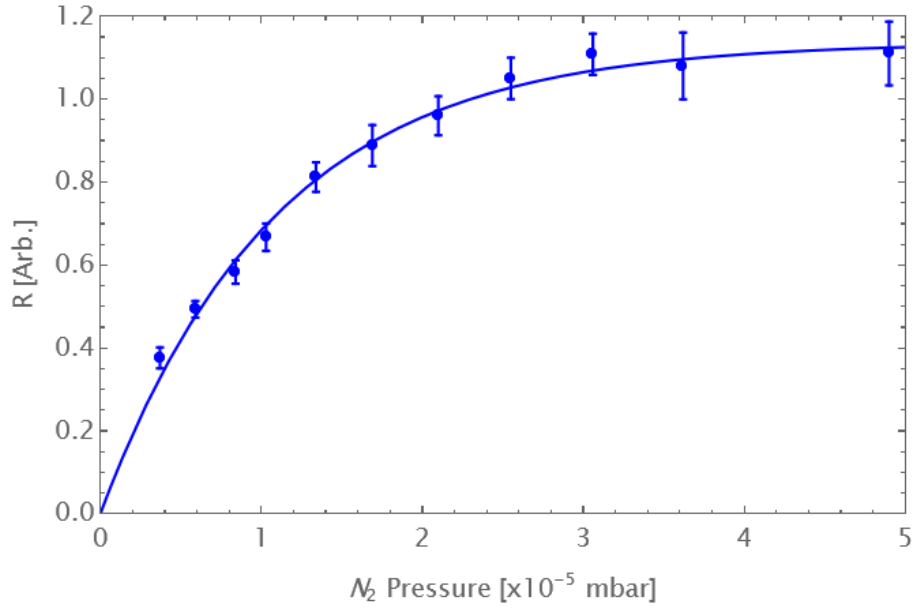
Figure 3.11: The rate of accumulation as a function of gas pressure, fitted to equation 3.8. Fitted parameters are $fI_0 = (1.14 \pm 0.02) \times 10^5$ and $D = 92100 \pm 4400$.
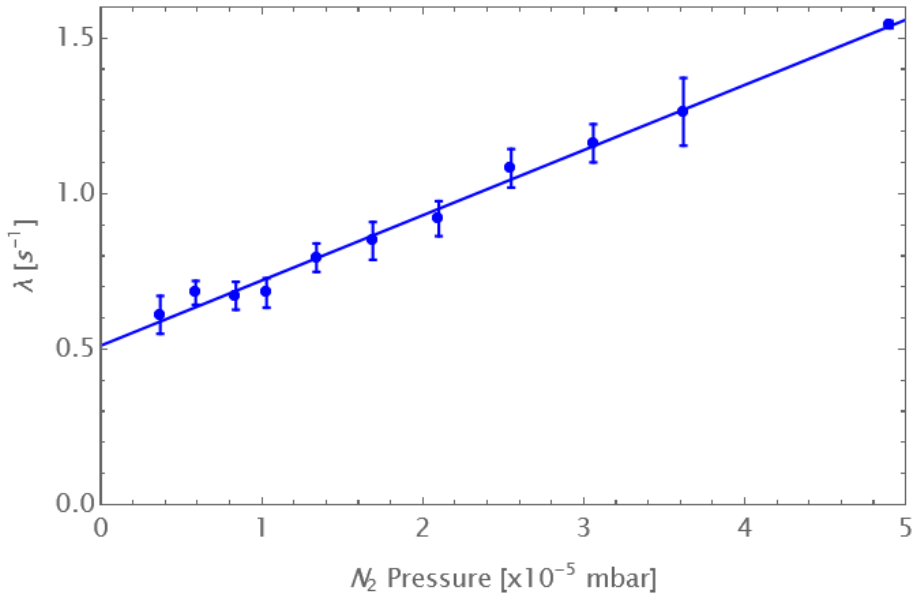
Figure 3.12: The loss rate as a function of buffer gas pressure. Fitted with the equation $\lambda = BP + c$ yielding $B = (21000 \pm 700)$ s^{-1}mbar^{-1}. The constant c is added due to annihilations on the background gas present.

shown in figure 3.14 to be 9.65 MHz.

Typical accumulation curves were performed to demonstrate the effect of the rotating wall on the number of positrons accumulated. Figure 3.15 shows two accumulation curves to demonstrate the rotating wall effect on accumulation, at a constant buffer gas pressure. Theoretically the rate of accumulation should be
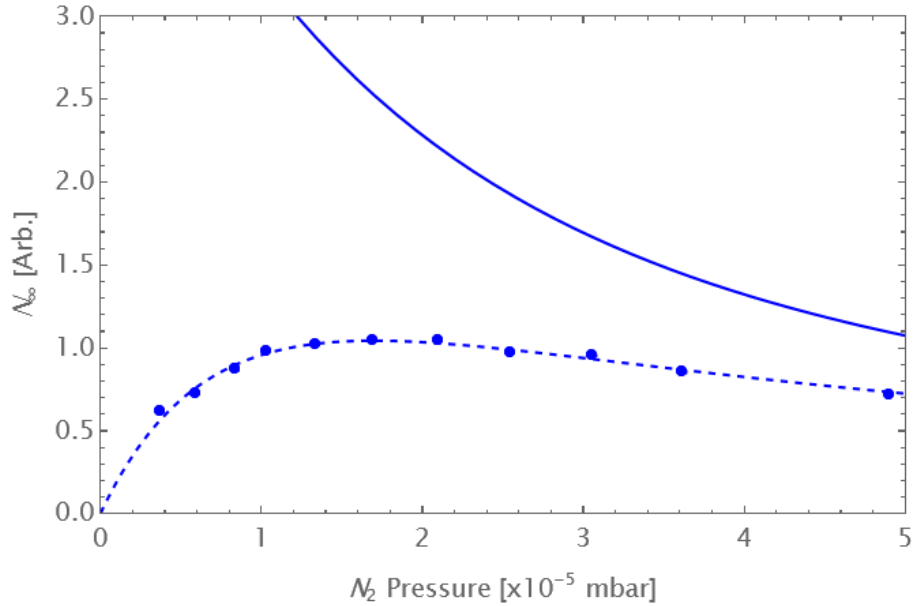
Figure 3.13: The saturation intensity as a function of buffer gas pressure, dotted line fitted with equation 3.12 and the solid line fitted with equation 3.11
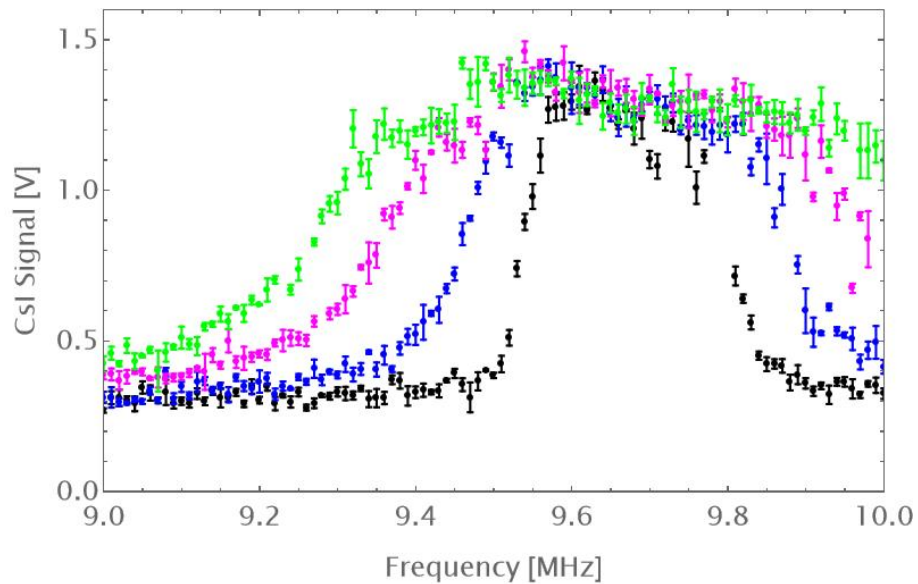
Figure 3.14: Rotating wall scan across frequencies 9-10 MHz for amplitudes 0.5 V (black), 1 V (blue), 1.5 V (pink) and 2 V (green).

equal [32], and the difference here is thought to be due to the data fitting. Figures 3.16 show the rate of accumulation and the lifetime as a function of the buffer gas pressure with and without the addition of the rotating wall. The comparison shows the loss rate is greatly reduced with the RW, most significantly as the pressure decreases, since the cloud is compressed and therefore the radial losses on the edge of the trap are being reduced [32]. However, there is a balance,

decreasing the pressure with the rotating wall reduced the rate of accumulation.
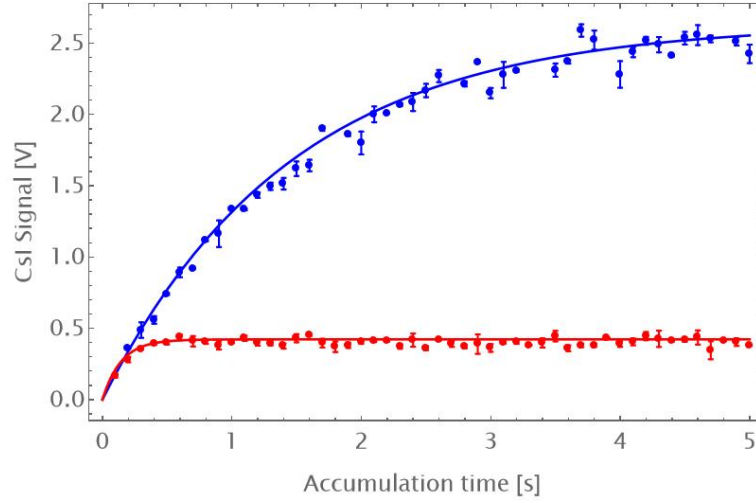
Figure 3.15: Accumulation curves where data is fitted with the equation 3.6. With no rotating wall applied (red) fitted parameters are $R = 2.92 \pm 0.28$ and $\tau = 0.14 \pm 0.01$. With rotating wall applied at a fixed frequency of 9.65 MHz and amplitude of 2 V, and the addition of a cooling gas (blue) fitted parameters are $R = 1.82 \pm 0.11$ and $\tau = 1.44 \pm 0.12$. A constant buffer gas pressure of 1.3 x 10^{-5} mbar was maintained.
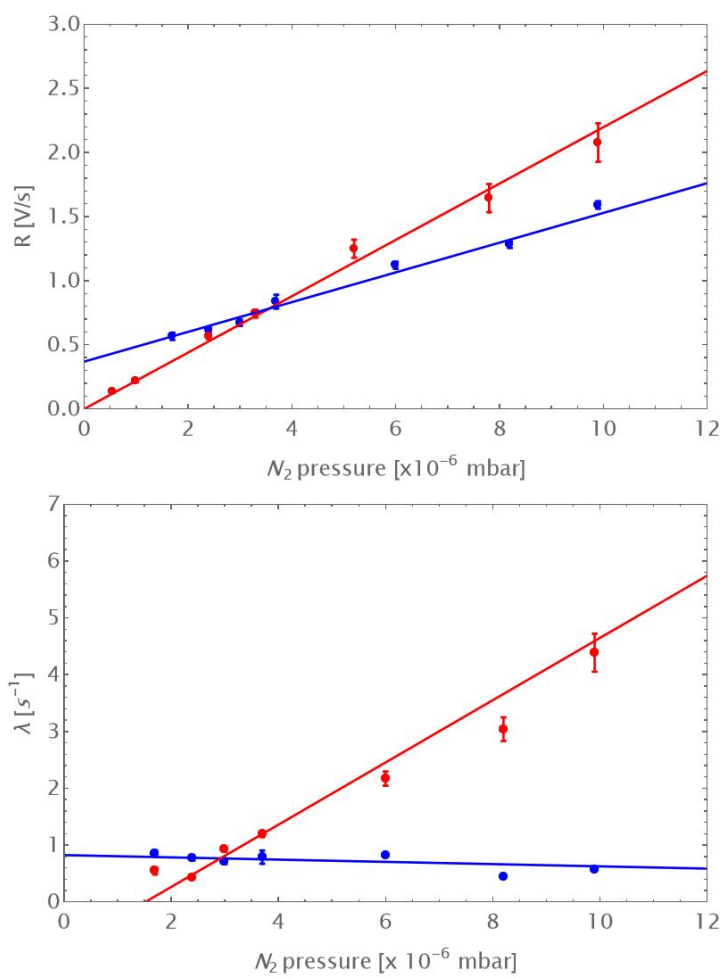
Figure 3.16: Top: The rate of accumulation with (blue) and without (red) the rotating wall. Bottom: Loss rate with (blue) and without (red) rotating wall.

Chapter 4

Positron Transfer

This chapter concerns the accumulation and ballistic transfer of particles from the two-stage to the third stage, with an understanding of the particle dynamics in the trap and the parallel energy spread of the cloud, with the goal of obtaining efficient transfer.

4.1 Accumulation Optimisation

To be able to successfully and efficiently re-trap a positron cloud in the third stage, consideration needs to be taken for the accumulation of the positrons in the two-stage buffer gas trap.

4.1.1 Accumulation Time

The first aspect to consider is accumulation time, with a view towards stacking of positrons and re-trap of large numbers. The figure 4.1 highlights the importance for short accumulation time to achieve the greatest rate of accumulation, and therefore one can achieve a greater number of positrons in a shorter time frame. The number of positrons increases linearly with accumulation time up to 500 ms, hence why from this point onward only an accumulation time of 500 ms will be used. The nitrogen buffer gas pressure is optimised between 1 and 1.3×10^5 mbar, for the highest rate of accumulation at this time.

4.1.2 Rotating Wall Optimisation

To increase positron yield in the two-stage accumulator, rotating wall techniques are utilised to reduce the losses in the initial stage of accumulation and to compress the cloud. The RW frequency that gives the greatest number of positrons is not always the frequency that enables highest compression rates. This property is a function of the rotating wall and slight asymmetries in the trap. Further details regarding this can be found elsewhere [33]. At 2 V amplitude of the RW, the number of positrons is seen to be the same for 9.4 MHz as well as 9.65 MHz in
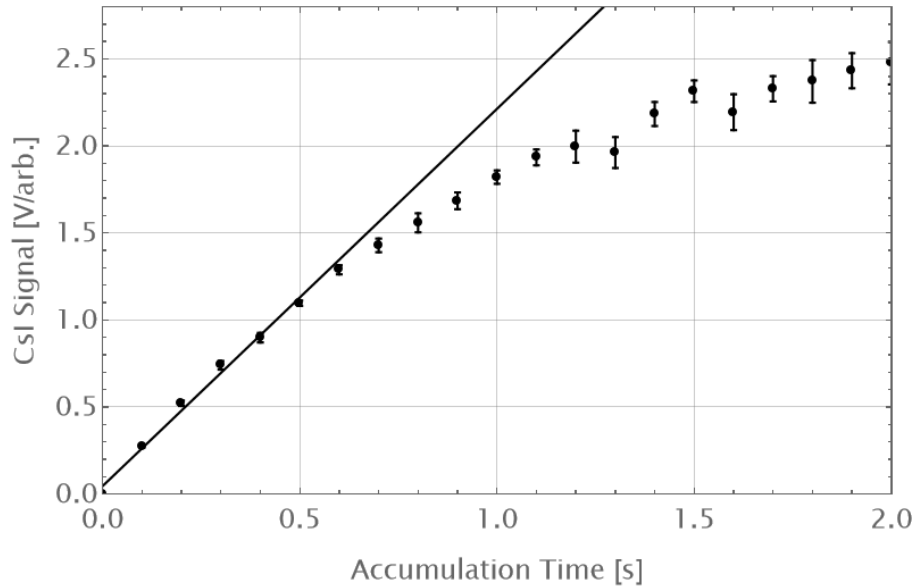
Figure 4.1: Accumulation curve with RW at a frequency of 9.65 MHz and 2 V amplitude. The straight line is to guide the eye to highlight the linear relationship between number of positrons and accumulation time that can be derived from equation 3.6
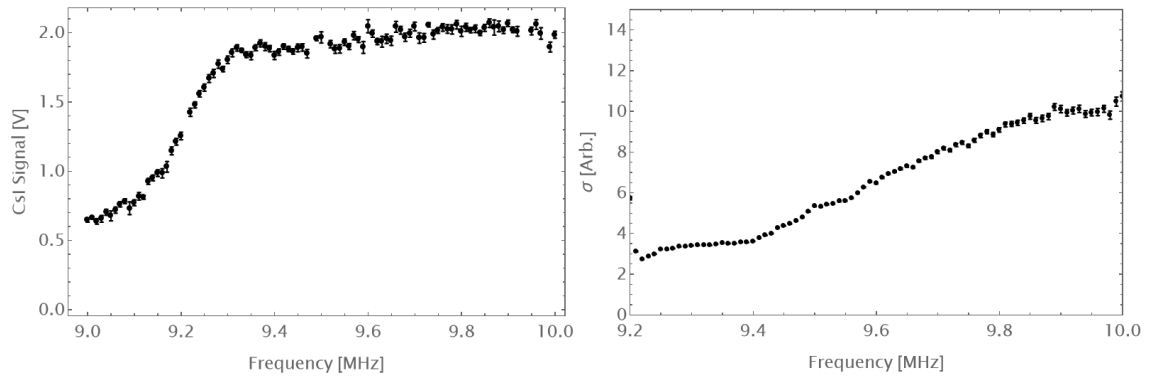
Figure 4.2: Left: CsI signal against RW frequency at an amplitude of 2 V. Right: The standard deviation in a Gaussian fit, relating the cloud width, σ, to the RW frequency.

figure 4.2, whilst the width of the cloud is much smaller; this small cloud was seen to be most appropriate for transfer, since the probability of parts of the cloud annihilating on any trap walls or transfer region are reduced due to its physical size.

4.2   Parallel Energy Measurements

A parallel energy measurement is used to obtain the kinetic energy distribution of the cloud, first developed for electron plasmas [34]. Here, 'parallel' is in relation to the trap axis and forward motion of the particles. This technique can be used for positrons held in a potential well within the two-stage accumulator, and are

ejected by lowering the potential (either slowly on the electrodes or using a fast pulse generator as described in the next subsection). A diagram of the potential well prior to ejection together with the ejection potential is shown in figure 4.3. A retarding potential applied to all third stage electrodes allows only particles,
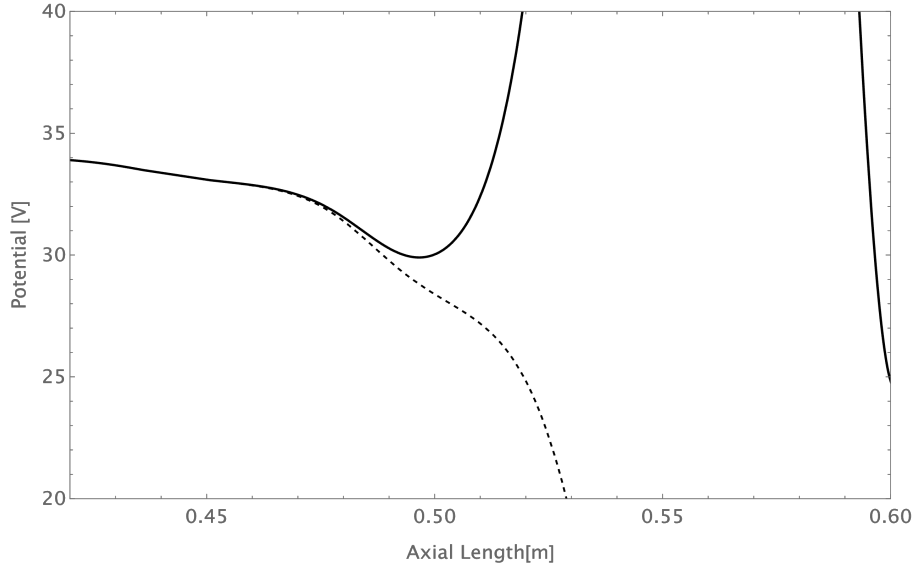
Figure 4.3: On axis potential well where particles are held in the second stage accumulator. The bottom of the well has a requested voltage of 28 V. The dashed black line shows the potential as it is dropped to eject particles. Potential calculated in Mathematica.

n, with energies greater than the retarding potential to be detected. Measurements taken over a range of retarding potentials give an integrated parallel energy measurement of the positron cloud. The energy distribution is assumed to be Gaussian, so the measurement can be fitted with a complimentary error function:

$$n(E) = \frac{N}{\sqrt{2\pi}\sigma} \int_E^\infty exp\left(\frac{-(E' - E_0)^2}{2\sigma^2}\right) dE' = \frac{N}{2} erfc\left(\frac{E - E_0}{\sqrt{2}\sigma}\right), \qquad (4.1)$$

where E_0 and σ are measures of the mean energy and energy spread. Measurements were taken of the energy distribution without any additional cooling wait. and with a 1 ms cooling wait added after accumulation time, with no rotating wall applied. The addition of the cooling wait reduces the energy spread by greater than a factor of 2, shown in figure 4.4.

4.2.1 Slow and Fast Pulsed Ejection

The parallel energy measurements taken with a retarding potential in the second stage are done so using a so called slow ejection by which the potential is lowered on the electrode. In regards to the transfer, the slow ejection is not useful since the fall time of the electrode potential from 140 V to 0 V is on the order of tens
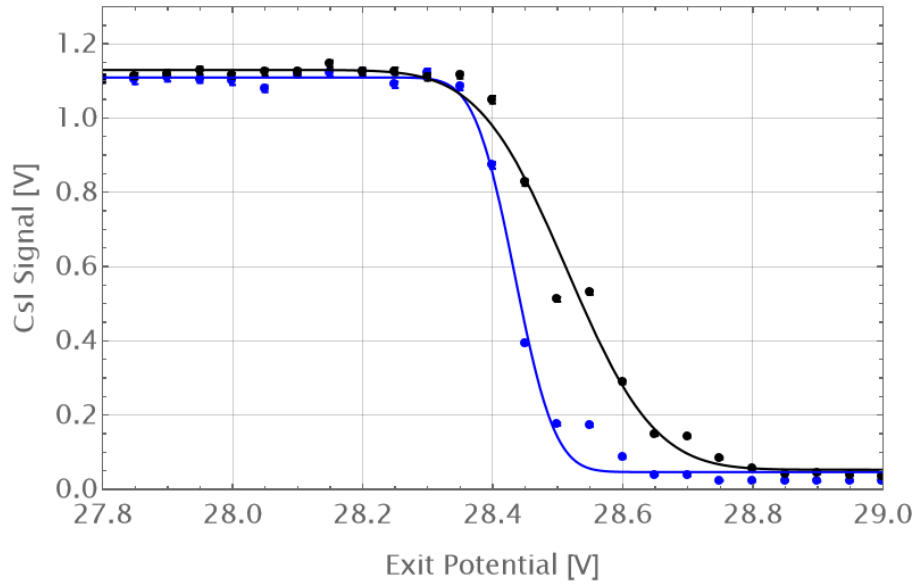
Figure 4.4: Parallel energy with no cooling wait (black) and after 1ms wait with no rotating wall applied (blue). Data fitted with an error function given by equation 4.1. Fitted parameters for no cooling wait give $E_0 = (28.514 \pm 0.006)$ eV, and FWHM $\Delta E = (0.208 \pm 0.017)$ eV. Fitted parameters with the cooling wait give $E_0 = (28.434 \pm 0.003)$ eV, and FWHM $\Delta E = (0.096 \pm 0.009)$ eV.

of microseconds. This relatively slow fall time creates a large transverse energy spread and therefore bunch length of the particles, and the work done here is yet to find a successful trapping mechanism to efficiently catch a cloud with slow ejection.

Two fast nanosecond high voltage pulse generators (fast pulsers) were trialled to control the voltage on the gated electrodes. The fast pulsers enable a smaller transverse energy spread when the particles are ejected, with a fall time of around 20 ns, and therefore can be re-trapped in the third stage trap. This parallel energy measurement is repeated with the fast pulsers connected to the end of the two-stage trap (E7) and the entry electrode of the third stage (E19). The resultant parallel energy measurement is shown in figure 4.5

The parallel energy spread using the fast gates is shown in figure 4.5. The data is normalised to the signal seen after positron accumulation with no interaction with the third stage electrodes. The energy spread of the particles is increased substantially through the use of the fast gates. This can be explained by recalling the potential well in figure 4.3 where the particles are held in the bottom of the well and they undergo simple harmonic motion. The fundamental nature of simple harmonic motion suggests that the particles spend the majority of their time at edges of the potential well where $v = 0$. At some time when the potential is lowered to that of the dashed black line in figure 4.3, the particles could leave the well in two distributions: one distribution from a proportion of particles on the
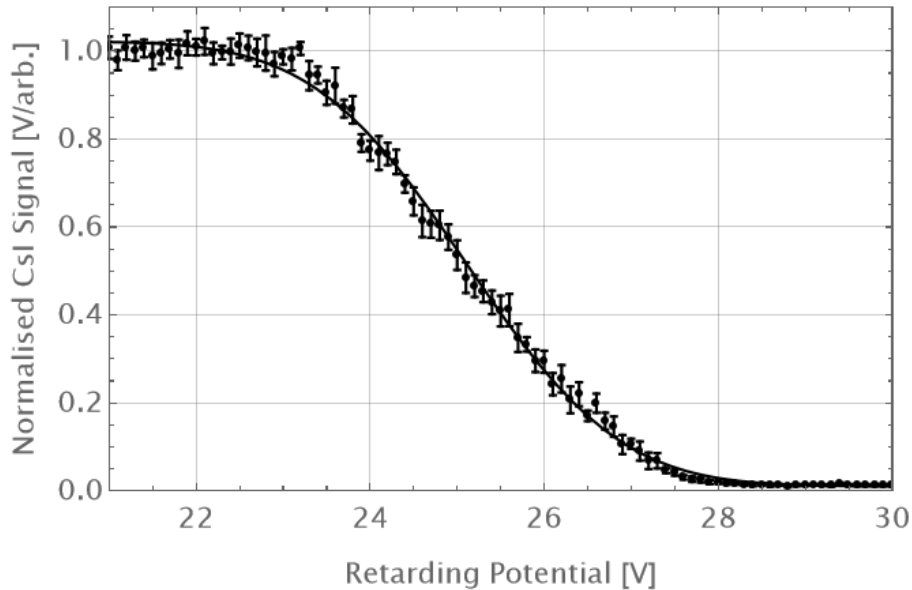
Figure 4.5: Parallel energy with the fast pulser for ejection. Data fitted with an error function given by equation 4.1. Fitted parameters give $E_0 = (25.11 \pm 0.02)$ eV, and FWHM $\Delta E = (2.72 \pm 0.05)$ eV.

left hand side of the well and the other from the right. It is thought that use of the fast pulser makes this effect more prominent. Since the potential is lowered so fast the particles can be 'dragged' down with the potential. The evidence to support this is the decrease in mean energy from 28.51 to 25.11 eV (plus their respective errors) from figures 4.4 and 4.5. The FWHM is calculated from the standard deviation in the Gaussian error function, given in equation 4.1.

4.3 SIMION Simulations

Simulations of particle transport throughout the beamline were conducted using a field and particle trajectory simulator, 'SIMION 8.0'. The software is commercially available and calculates the electric fields given by a specific user defined geometry by numerically solving the Laplace's equation and the trajectories of the particles are traced with various parameters available to record such as kinetic energy and three dimensional position of each particle. Further details about the SIMION software package can be found in reference [35].

4.3.1 SIMION Program Details

Relevant sections of the beamline were recreated in a geometry file ('.gem') with the correct electrode lengths and widths for the second stage accumulator electrodes, the third stage electrodes, and a target. The first stage accumulator electrodes are ignored for the purposes of these simulations since the interesting

physics examined is after the release of particles from the second stage accumulator to the third stage and target underpinned by the transfer dynamics. Hence, aspects such as the cooling gas and rotating wall are also ignored and the simulations begin at a stage theoretically after particles have been compressed and cooled into the potential well of the two-stage accumulator. SIMION interprets the geometry files to create potential arrays which are refined to produce a similar virtual environment to the experimental setup, with the approximate applied electric and magnetic fields. A user program ('.lua' file) is then written to determine the actions of particles and create loops for batch measurements [27].

4.3.2 SIMION Energy Measurements

Particles are initiated in the well of the second stage accumulator with a given energy spread. To be able to compare the parallel energy measurements with experiments, the particles are left 'to fly' (to be ejected from the well) and the kinetic energy is measured when each particle reaches the target of the beamline. The data collected from this simulation is a file containing the particle number, time of flight, position and kinetic energy at the time of termination. From this, a histogram can be produced from the kinetic energies. The data can be analysed to find various parameters such as the mean, standard deviation and spread, and therefore can be used to plot a cumulative distribution function to compare to the experimental data. The result is given in 4.6. The value for E_0 from the simulation is in very good agreement with experiment. The spread is said to be in fair agreement since the value of the FWHM slightly greater in the simulation than the real data; the data has a sharper drop than the curve fit from the simulation where the particles begin to escape the well at around 23 V. This implies that the positrons from the experimental data have started to thermalize in the well. There could also be a slight discrepancy in the amplifier rise time between the simulation and experiment, which could be a source of improvement.

4.4 Transfer and Re-trapping Experiments

A 'catch and expel' timing scan was first performed to ensure that transfer of positrons from the second stage to the third stage is occurring and therefore find an optimum transfer time δt. An illustration of the experimental sequence is shown in figure 4.7, along with a description of the sequence details in table 4.1. If the transfer time δt is too short, the positrons do not make it through to the third stage at all to annihilate. If the transfer time is too long, the positrons bounce back and are not re-trapped in the third stage either. The first peak in figure 4.8 corresponds to positrons that are re-trapped in the third stage at an optimum transfer time of around 550 ns. There are several peaks, where the positrons bounce back and forth between the potential barriers, and the amplitude of the peaks decreases in response to the losses that occur due to annihilations.
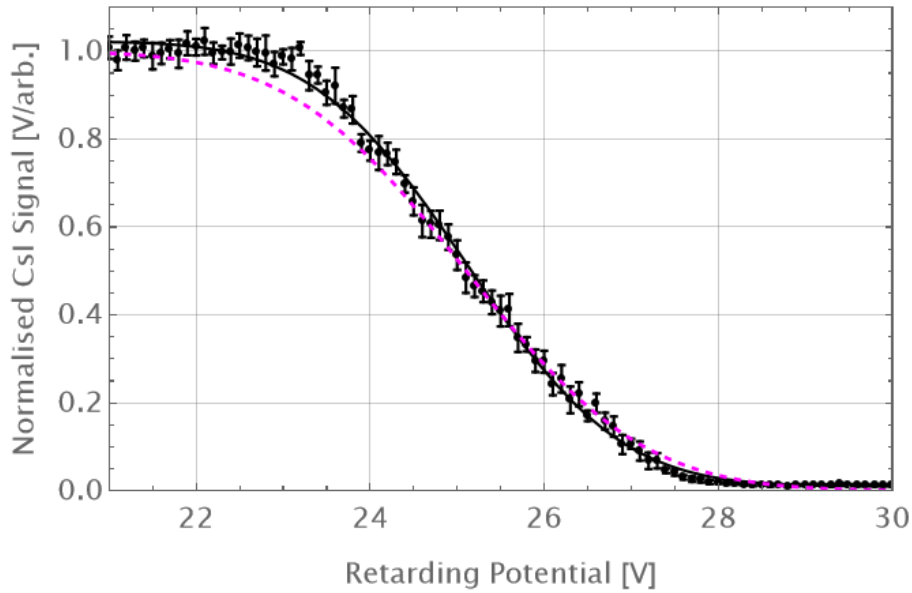
Figure 4.6: Parallel energy with the fast pulsers for ejection and simulation data given by the purple dash fitted line. Simulated fitted parameters give $E_0 = (25.10 \pm 0.02)$ eV, and FWHM $\Delta E = (3.13 \pm 0.04)$ eV.

The peaks also increases in width as the transfer time increases, where the cloud has axially spread out during the transport and therefore the transverse energy spread increases. Initially, all of the voltages on the third stage were set at 0 V, apart from the two end electrodes that are used as gates (140 V) creating a flat bottomed square potential well. Data was recorded from two CsI detectors to yield information on where any losses occur. One detector was placed at X4 at the end of the beamline and the other at X2 at the end of the 2-stage accumulator (refer back to figure 3.3). If particles were being lost at the entry gate, an annihilation signal would show on X2. The results are in figure 4.8.

The catch and eject timing scan was then performed again for differing flat bottom potential well heights of 0 V, 10 V and 20 V. The results are shown in figure 4.9, and one can infer much about the particle motion as the receiving well height is varied. Figure 4.9 shows that as the receiving potential well is increased from 0 to 20 volts, the particles are detected at slightly later relative times due to the particles having a reduced kinetic energy. The peaks that correspond to particle detection also have an increased relative width also due to the reduced kinetic energy. It is inferred that a receiving well potential that approaches the mean energy of the incoming cloud slows the positron cloud down. Following this, it is suspected that a successful, efficient transfer occurs when the receiving well matches the ejection cloud parameters.

A timing scan for the transfer was repeated as before in figure 4.10, but for increasing receiving well heights that approach the incoming energy of the cloud
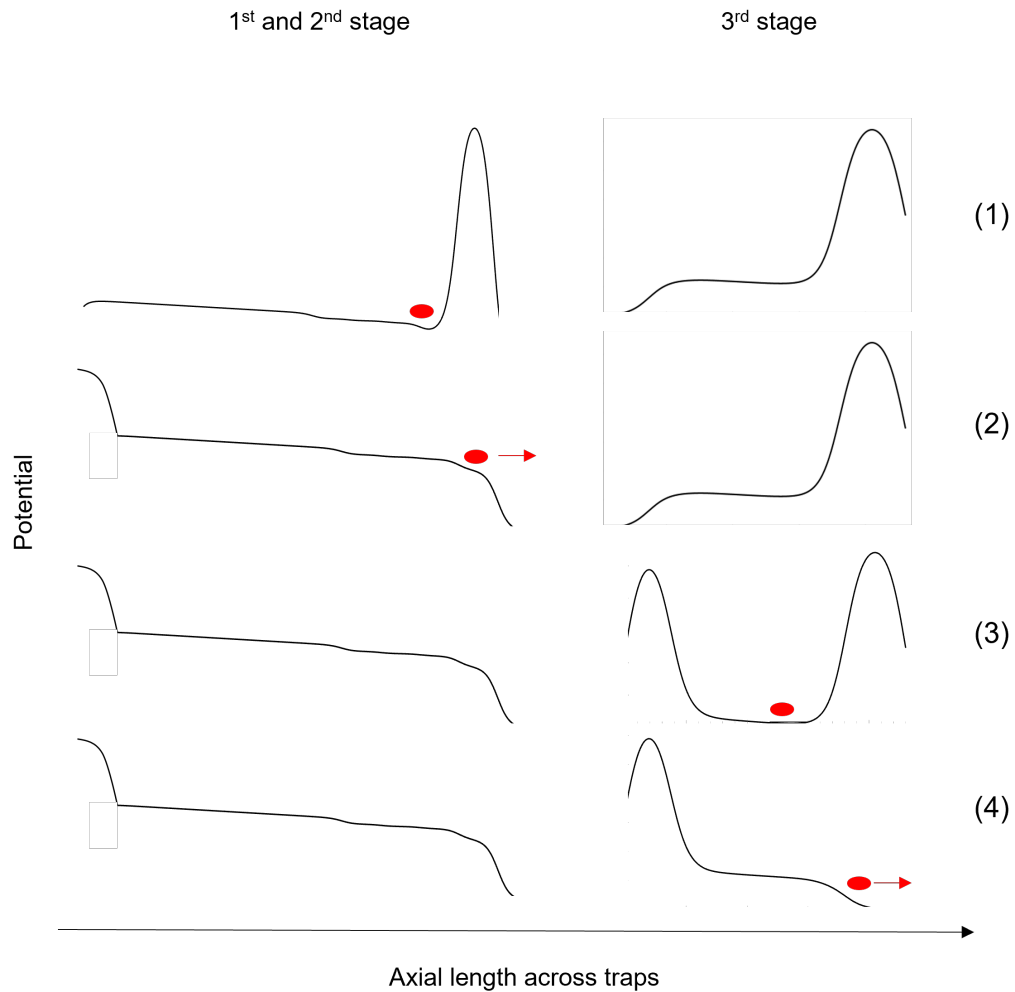
Figure 4.7: Illustrative schematic of the trap potentials during a transfer sequence. The numbered lines correspond to the analogue output lines used in the sequence editor given in chapter 3. The table 4.1 details the analogue output lines further.

during transfer. It can be seen for receiving well potentials of up to 22 V the behaviour is as expected, where the relative peaks are shifted to the right, increase in relative width and decrease in signal due to the reduced kinetic energy and losses between the traps in subsequent motion that is observed. The unusual behaviour that is displayed for 25 V and 27 V is due to the fact the incoming positrons have an approximately equal energy, therefore are left with very small amounts of kinetic energy as the positrons enter the potential well. For the application of trapping, this is good since the reduction in kinetic energy allows the positrons to be trapped with fewer looses due to the fact that the particles with greater energy could escape the axial potential.

Table 4.1: Table showing the sequence details relating to the illustrative schematic in figure 4.7.

Output line	Duration	Sequence details
1	500ms	Positrons accumulated with RW on
2	δt	Potential lowered on the last electrode of the second stage (E7) with fast pulser allowing positrons to become ejected
3	$10\mu s$	Potential raised on first electrode of the 3rd stage (E19) with fast pulser and particles (if present) become trapped in the 3rd stage
4	100ms	Potential lowered on last electrode of the 3rd stage allowing trapped particles to be ejected and annihilate on target. Trigger digitiser and camera virtual instruments
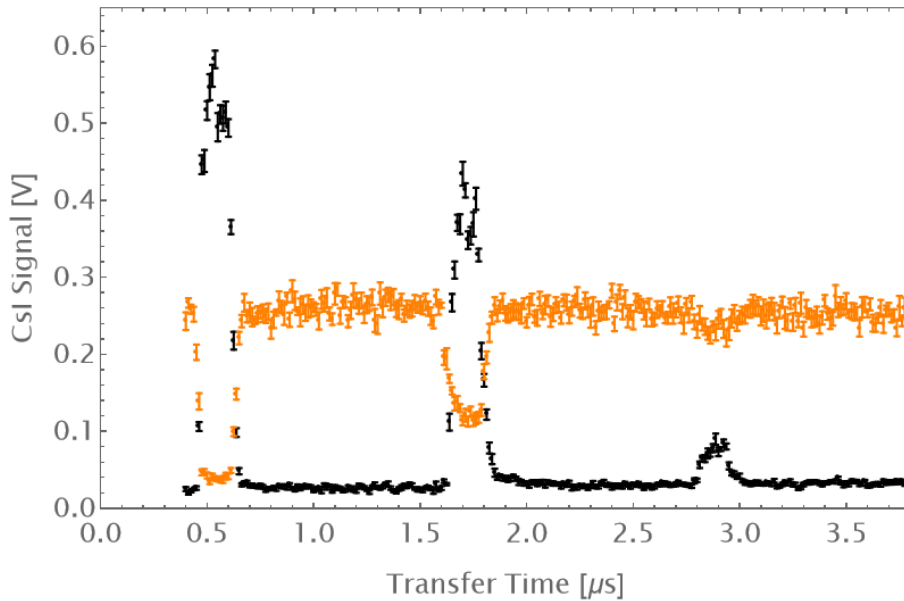
Figure 4.8: Initial timing scan completed for a square flat bottomed well at 0 V, with positrons detected at the end of the beamline at X4 (black) and the positrons detected at the end of the 2-stage (orange). The optimum transfer time δt is determined 550ns.

4.5 Conclusions from Single Cloud Transfer

Manipulations of the well were made, with knowledge of the incoming cloud energies as described in this chapter. A stepped potential was found to be more appropriate, since a flat well results in a lifetime on the time scale of millisec-
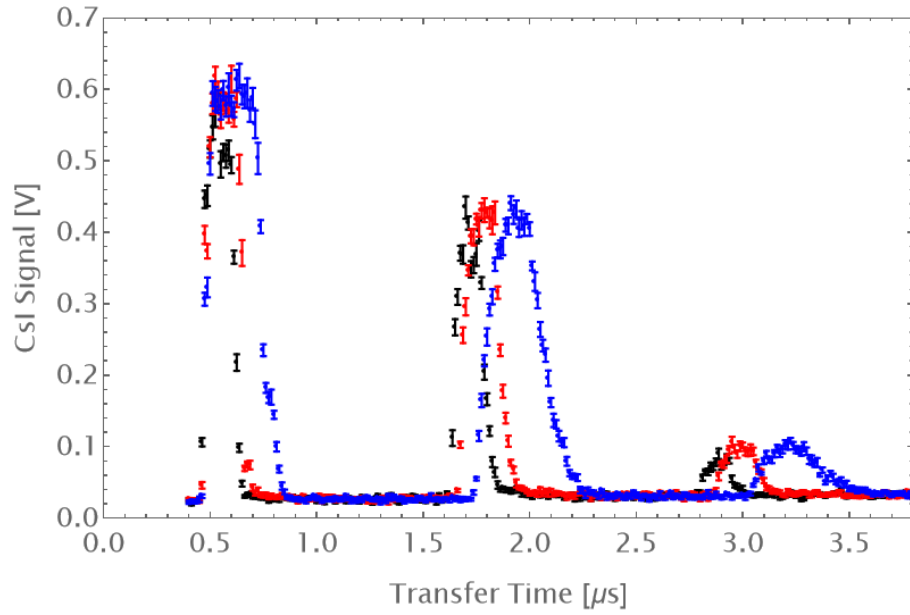
Figure 4.9: Catch and eject transfer timing scan for differing potential well heights; 0 V (black), 10 V (red) and 20 V (blue).
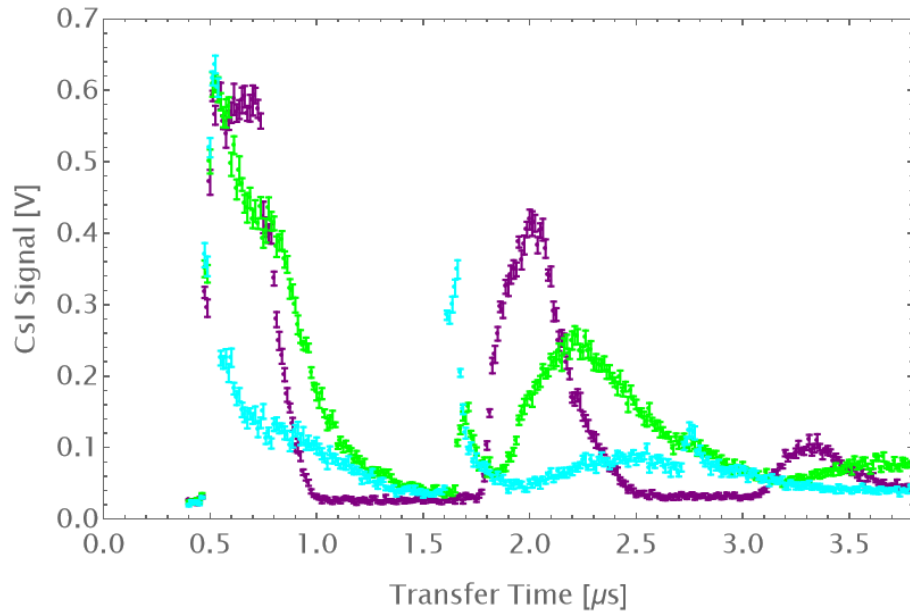
Figure 4.10: Catch and eject transfer timing scan for differing flat bottom potential well heights that approach the incoming energy of the cloud; 22 V (purple), 25 V (green) and 27 V (light blue).

onds. A candidate well is shown in figure 4.11 with a receiving potential just below the lowest incoming energies from the parallel energy measurement and a shallow potential well, with corresponding positron lifetime shown in figure 4.11.
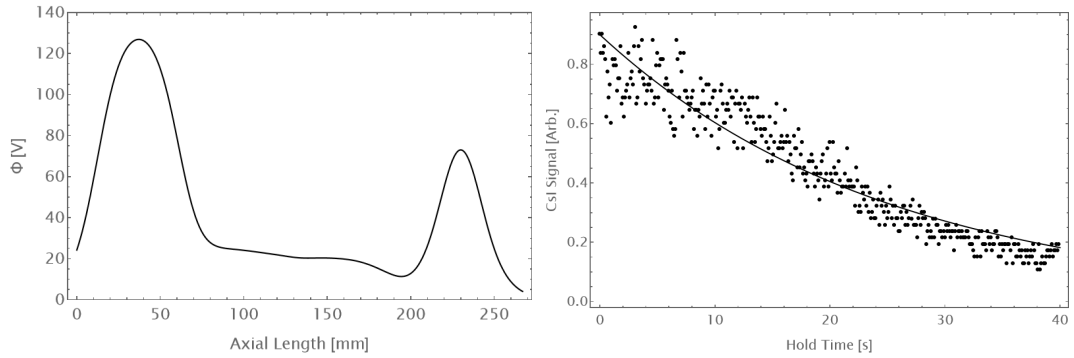
Figure 4.11: Left: The potential well adopted in the third stage, calculated in Mathematica. Right: Lifetime curve fitted with equation 3.7 yielding $\tau = 25.04 \pm 0.47$ s

From the transfer and re-trapping experiments, knowledge of what makes a 'good' transfer was accumulated. A 'good' transfer would be defined as particle transport from the second stage buffer gas trap into the third stage trap, with minimal charge losses, maintaining a high central density and a suitable lifetime. A good transfer must have a receiving well that is similar to the ejection cloud in parallel and transverse energy. The final transfer efficiency is calculated by taking a measurement of the CsI signal prior to transfer, and again after a transfer with a 10μs trap time (sufficient to have trapped particles). The data from those measurements is shown in figure 4.12 with a mean and standard error.

Once optimised with the experiments performed in this chapter, a transfer efficiency of (96.6 ± 2.8) % is achieved, with a trapping lifetime of 25 seconds.
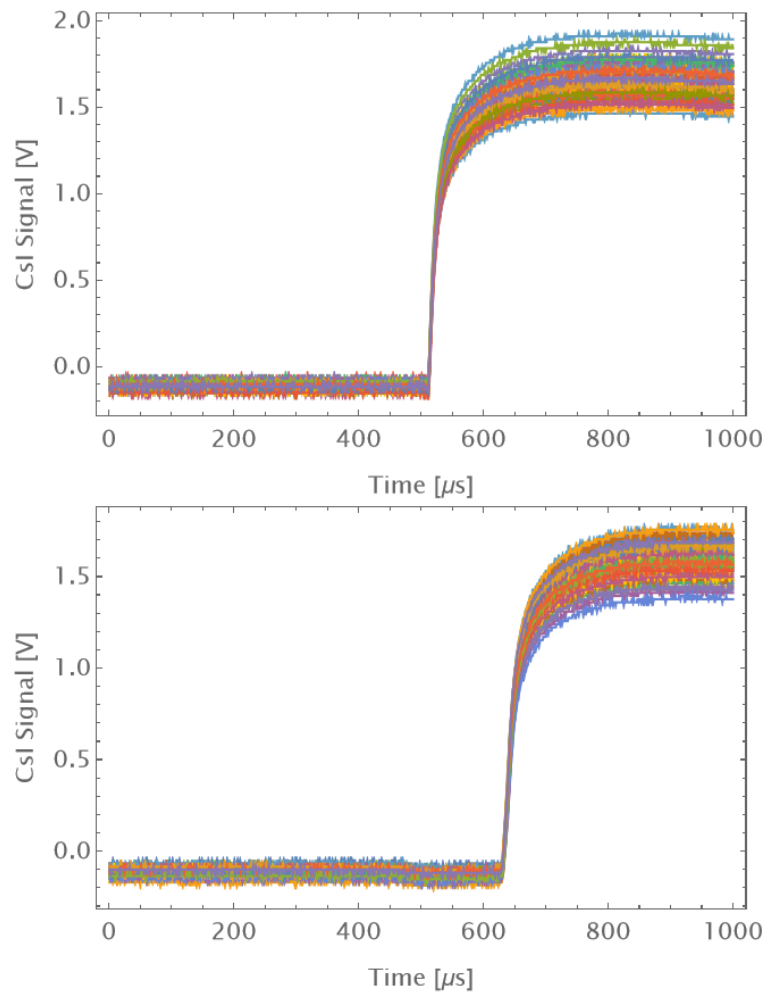
Figure 4.12: Top: 50 repeat measurements of the Ceasium Iodide signal (proportional to the number of positrons) before transfer, with CsI signal = (1.788 ± 0.01) V. Bottom: 50 repeat measurements of the CsI signal after transfer and trapping, with CsI signal = (1.728 ± 0.01) V.

Chapter 5

Magnetron Orbit Excitation for Transfer

Magnetron orbit manipulations have been previously studied in the two stage accumulator by Mortensen, with a full theoretical model and excellent experimental agreement [36]. This chapter describes the use of magnetron orbit excitation to adjust the clouds injection position relative to the third stage trap center, to overcome misalignment. Further understanding of the particle dynamics in the trap is attempted when utilising this technique to inject off-axis, through the use of cloud expansion and lifetime data.

5.1   Trap Misalignment

It was found that the two traps (two-stage accumulator and third stage trap) were misaligned. This resulted in the transfer process to have a short lifetime < 8 s, due to the off axis transfer enabled by this misalignment. The two-stage ejection leaves a cloud on an MCP position ($x = 92, y = 58$ pixels) as shown in figure 5.1. After transfer, the cloud was imaged on the MCP and is shown in 5.2. It was concluded that the center of the third stage trap was roughly ($x = 120, y = 65$) pixels, therefore the trap centers are misaligned by approximately 7.5 mm, which caused the particles to be imaged as a ring due to the magnetron frequency. The misalignment is thought to be from the movement of solenoid 3. The magnet would need to be aligned again, however this presented an opportunity to use the magnetron orbit excitation that allows manipulation of the cloud position prior to ejection from the two-stage accumulator, to overcome this trap misalignment.
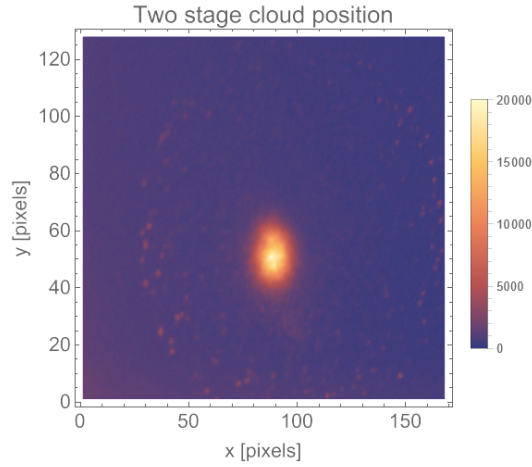
Figure 5.1: The imaged cloud as ejected from the two stage accumulator. The cloud position is fitted with two Gaussian distributions to extract center (x = 89, y = 51) pixels. The colour ramp represents the intensity.
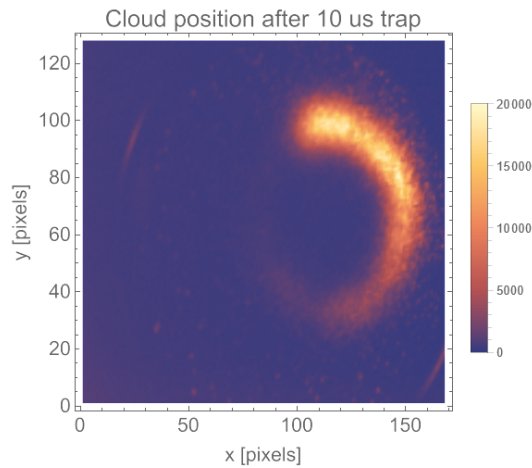
Figure 5.2: The imaged cloud displaying magnetron motion in the third stage after being transferred and held for 10 μs. The colour ramp represents the intensity.

5.2   Magnetron Orbits

The principle of magnetron orbit manipulation is to radially offset the cloud position. A schematic of the two traps and the magnetron excitation is shown in figure 5.3. By distorting the well with the addition of an external bias to opposing electrodes, V_b, the trapping potential is modified, shifting the extrenum, given by the black crosses. With the bias applied, the cloud orbits on a trajectory following the green dashed line. The external bias is removed, restoring the original trapping potential, so the cloud will orbit around the original trap center for a time t_2 on the red dashed line, to achieve a desired final position of the cloud. The final cloud position can be imaged by rapid ejection onto the MCP, but is seen here as method to control the injection position of the cloud into
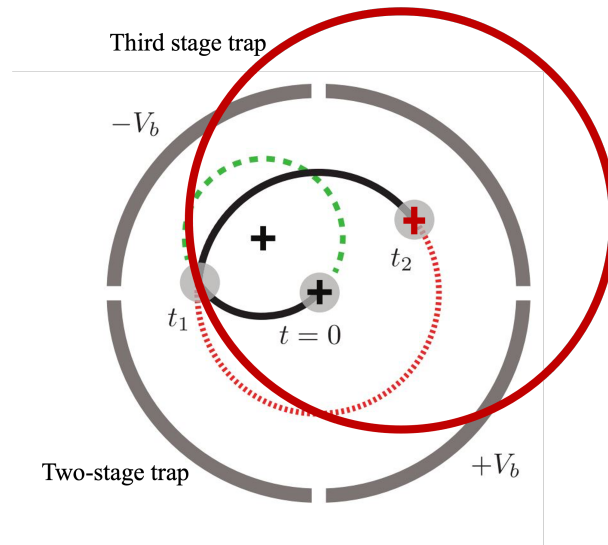
Figure 5.3: A cross sectional overlay of the two traps, showing the RW electrode in the two-stage accumulator (grey) and the third stage trap electrode (red). The bias is applied to opposing quadrants and the first and second magnetron orbit is shown for time periods t_1 and t_2. The red cross corresponds to the center of the third stage. Figure adapted from [36].

the third stage. The dependency of the injection position is investigated through cloud expansion and lifetime.
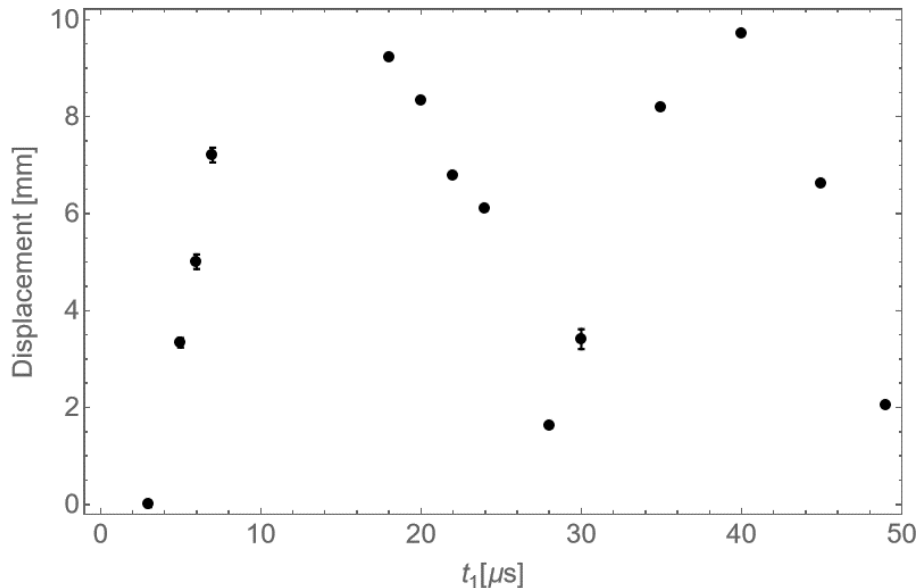
Figure 5.4: The displacement of the cloud for times t_1 and a voltage bias of 1.4 V

Figure 5.4 shows the displacement of the cloud for the various time t_1, where the period of the orbit is 26 μs. The section between 8 and 18 μs has no data points due to the damage on the MCP screen, therefore the cloud could not

be imaged. From this measurement, a range of times $8 < t_1 < 20$ μs were experimentally tested. A combination of t_1, t_2 and V_b was chosen to manipulate the cloud position to the third stage trap center.

5.3   Magnetron Orbit Controlled Transfer

The value R_{inj} is the radial injection position, where $R_{inj} = 0$ is the center of the third stage. An off axis transfer is achieved by slightly altering the parameters V_b, t_1 and t_2 so that $R_{inj} > 0$.

Figure 5.5 shows the imaged positrons at different trap injection positions after 10 μs. When the particles are injected off axis, they appear in a ring shape due to the magnetron motion where some particles are 'dragged'. The smearing is because of the non-ideal trapping potential, resulting in small differences in the magnetron frequencies across the cloud diameter.
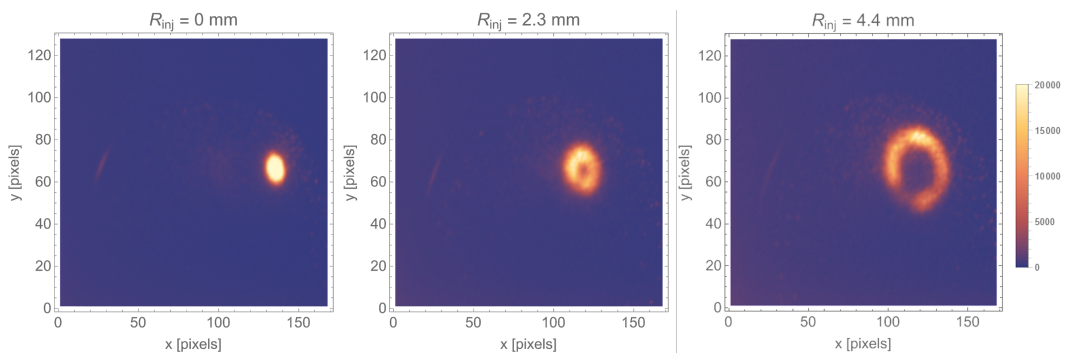
Figure 5.5: MCP images showing the motion of the cloud, when trapped in the third stage, affected by the injection radius relative to the center of the trap. The colour bar is the relative intensity. One pixel = 0.27 mm.

5.4   On Axis Expansion

The expansion rate is dependant on the position the cloud injected relative to the centers of the two traps. For on axis transfer, the center of the third stage trap can be extracted from a Gaussian fit where the cloud is represented by a single point of charge and the values of x_0 and y_0 for the Cartesian coordinates for the center of the third stage are found from

$$G(x,y) = A \exp\left(- \frac{(x - x_0)^2 + (y - y_0)^2}{2\sigma^2} \right), \tag{5.1}$$

where A, x_0, y_0 and σ are fit parameters. Therefore, the expansion rate is obtained by fitting images for increasing hold times, shown in figure 5.6. It is seen that for on axis transfer, there are two distributions in the rate present, where the data

is fitted with linear fit lines. The rapid expansion rate for times $0 < t < 150$ ms is given as (1.08 ± 0.10) mm s^{-1}. The second slow expansion rate for times $150 < t < 1000$ ms is given as (0.033 ± 0.006) mm s^{-1}. This indicates the cloud is not expanding and annihilating on the trap walls (radius of electrodes = 20.5 mm). Further modelling would be required to understand this difference in expansion rate for times < 150ms.
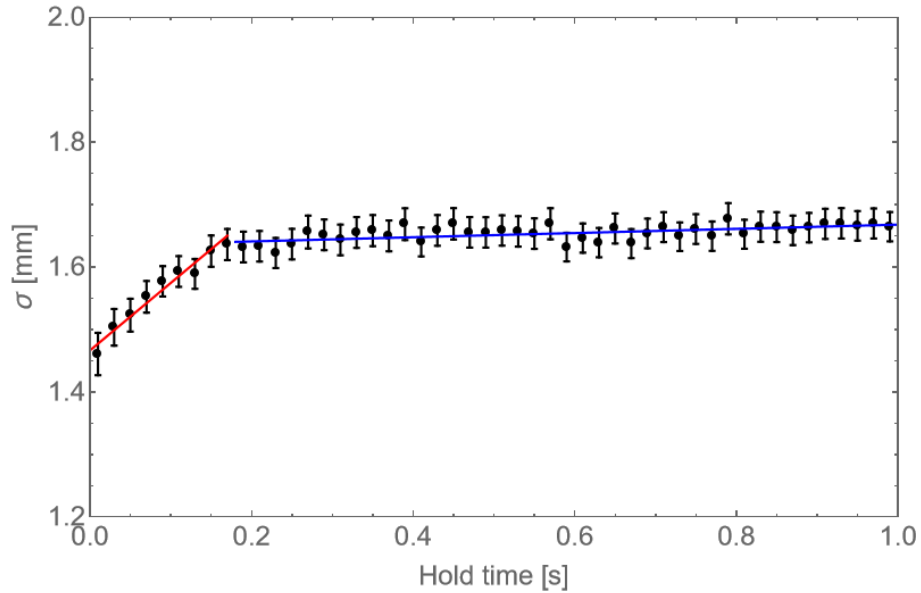
Figure 5.6: A measure of the cloud width σ for hold times up to 1s. There are two distributions which are both fitted with linear fit lines that yield expansion rates of 1.08 ± 0.10 mm s^{-1} (red) and 0.033 ± 0.006 mm s^{-1} (blue).

5.5 Off Axis Transfer and Expansion

To be able to look at the effect of transferring a cloud off axis, a method was developed to characterise the injection point relative to the trap positions. The data in Cartesian coordinates was converted into radial coordinates where $R = \sqrt{(x - x_0)^2 + (y - y_0)^2}$, with x_0 and y_0 as the coordinates of the center of the trap. When the cloud appears in a ring shape (as in the right image in 5.5), the distance from the center of the trap, R_{inj}, can be found from summing the mean intensities at a value of R. Fitted by a one dimensional Gaussian like fit,

$$G(R) = A \exp\left[-\frac{1}{2}\left(\frac{|R - \mu|}{\sigma}\right)^k\right],\qquad(5.2)$$

where A, σ and k are fit parameters, and μ is the radial distance from the particles and the center of the third stage trap. For an off axis injection, the mean intensity as a radial function is shown in figure 5.7, from which the injection radius can be extracted. Note the data to the left of the Gaussian fit is sitting
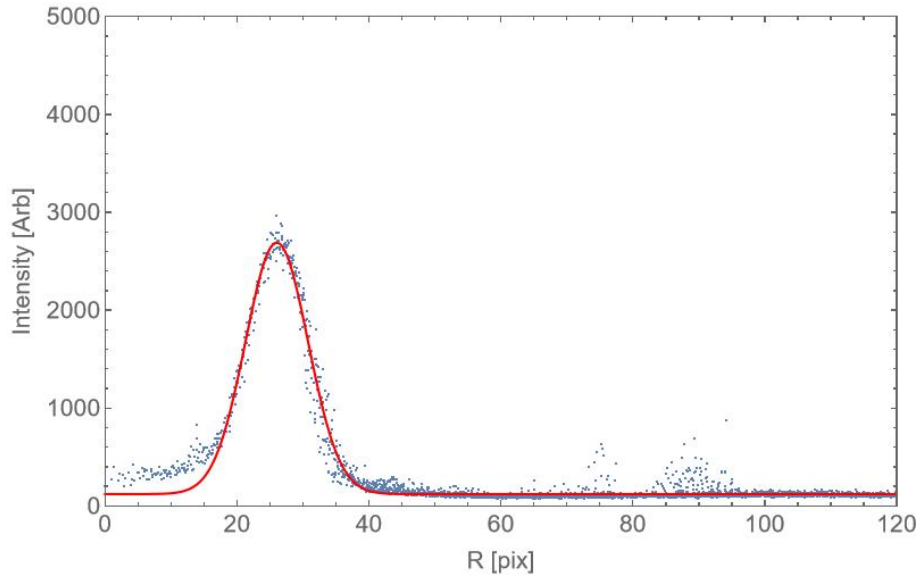
Figure 5.7: The mean intensity as a radial function for off axis transfer, held for $10\mu s$, producing an off axis transfer. The data is fitted with equation 5.2 (red) and the fit parameter μ yields the value $R_{inj} = 7$ mm.

at greater intensities due to axiallisation and inward transport of particles in the trap, therefore the Gaussian like fit is an approximation.

An attempt to characterise the expansion rate of the cloud when it was transferred off axis was made. Particles were held in the third stage for various times up to 500ms, and for 2 different injection radii, 0.6 mm and 1.93 mm. As time increases the cloud is seen to expand and axialise. This is repeated for various hold times in between to measure the widths of the cloud. The results are plotted in figure 5.8. When the radial injection position is further away from the trap center, there is a larger final width of the cloud. Further modelling or simulations would be required to gather quantitative data from the expansion measurements or to be able to mathematically fit the trends observed.
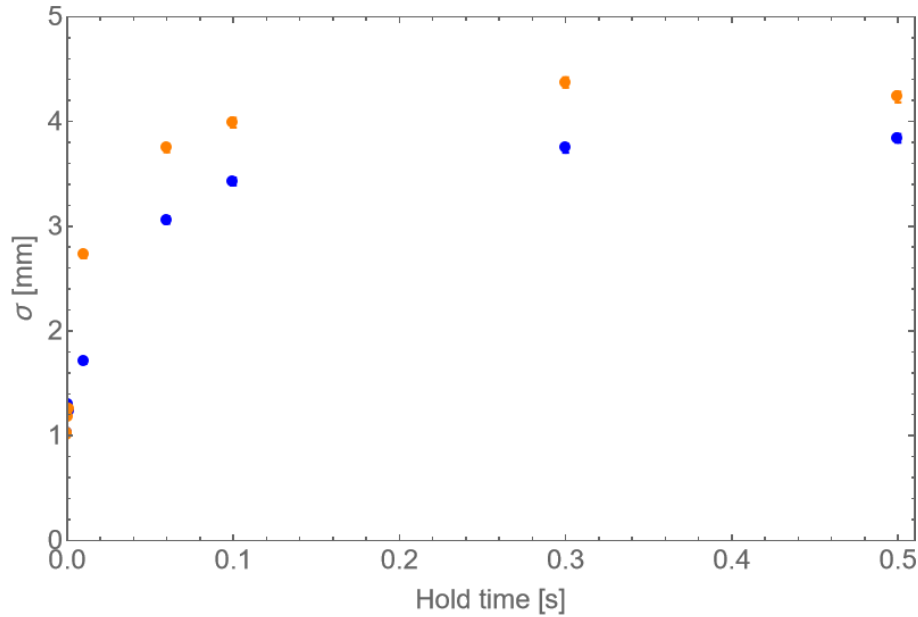
Figure 5.8: A measure of the cloud widths σ for increasing hold times up to 500 ms for injection radii 0.6 mm (blue) and 1.93 mm (orange).

5.6   Lifetime Measurements and Charge Losses

When using the magnetron orbit manipulation in the two-stage accumulator to prepare the cloud for transfer, particle losses occur, therefore resulting in a recapture efficiency of between 60-70 %. The reason for this is not yet fully understood. It was suspected that the magnetron orbit manipulation gave rise to a so-called halo. The term 'halo' in a physics context (often used in plasma physics), regards to particles that sit outside the area of central density, in a ring shape symbolic of a halo. MCP images suggested there was a halo present, but a calibration of the pixel/volt would be needed to further explore this hypothesis, which was not achieved here.

A lifetime decay measurement was taken by trapping the cloud for increasing hold times up to 10 seconds once transferred, and the mean trapping lifetime can be obtained by fitting the data with 3.7. A two component lifetime was observed, with a short lifetime at < 100 ms. This behaviour has been seen many times historically on the Swansea apparatus and the reason is not yet fully understood. In this measurement, it is suspected that the halo previously described rapidly expands and annihilates on the walls of the trap, leaving the remaining cloud with the secondary 'long' lifetime, which better represents the results of the experiment. The (long) trapping lifetime for an on-axis transfer is shown in figure 5.9, and was seen to increase from what was shown previously in chapter 4.

The halo that is thought to be the cause of rapid particle loss is an artifact of
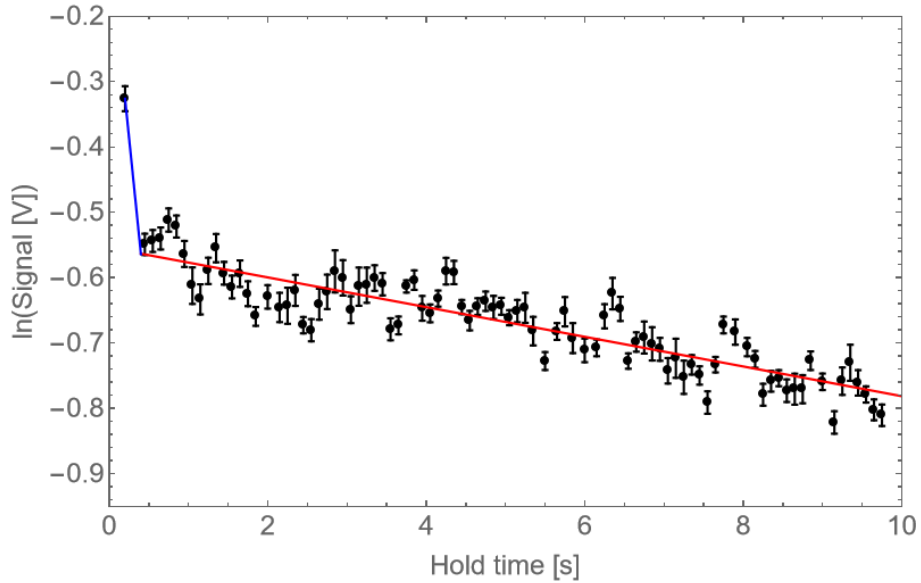
Figure 5.9: Natural logarithm of positron number as a function of hold time in the third stage. The data points are the mean and standard error of 3 repeat measurements, the two component lifetime was fitted with equation 3.7. The linear fit (blue) gives the trapping 'short' lifetime $\tau_1 = 0.84$ s. The linear fit (red) gives the 'long' trapping lifetime $\tau_2 = (44.03 \pm 3.22)$ s.

the system, and with slight changes to the system environment (coil or solenoid movement) the halo may not be present. Without the magnetron orbit manipulations, there is no indication towards a halo. From the data available, it is reasonable to assume that those losses would not occur with an aligned system that subdues the need for magnetron orbit manipulations.

As the cloud is injected further off-axis, there is a significant deterioration in the lifetime. Figure 5.10 shows the measurements of the lifetime as a function of the radial injection position. The decrease in lifetime is due to the increased annihilations on the trap electrodes as the magnetron radii increases.
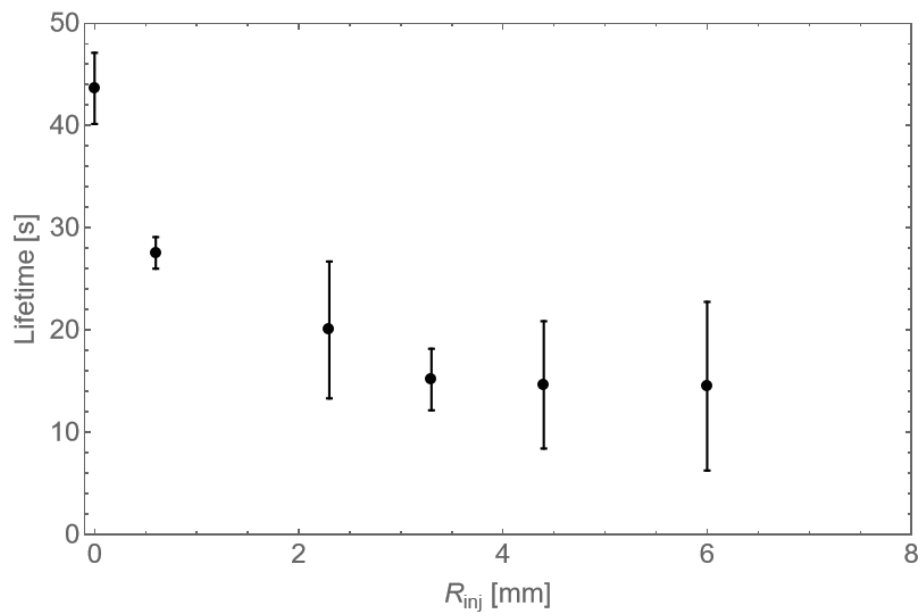
Figure 5.10: The lifetime for different injection positions of the cloud in relation to the third stage trap center.

Chapter 6

Positron Cloud Mixing and Stacking

This chapter further explores re-trapping in the third stage. The interactions between multiple clouds are investigated by measuring the expansion rate and the influence of the clouds position in the trap on the lifetime. Ideas to generate large numbers of positrons are presented through the stacking technique, where multiple clouds are transferred and trapped with high efficiencies.

6.1   Third Stage Parallel Energy Measurements
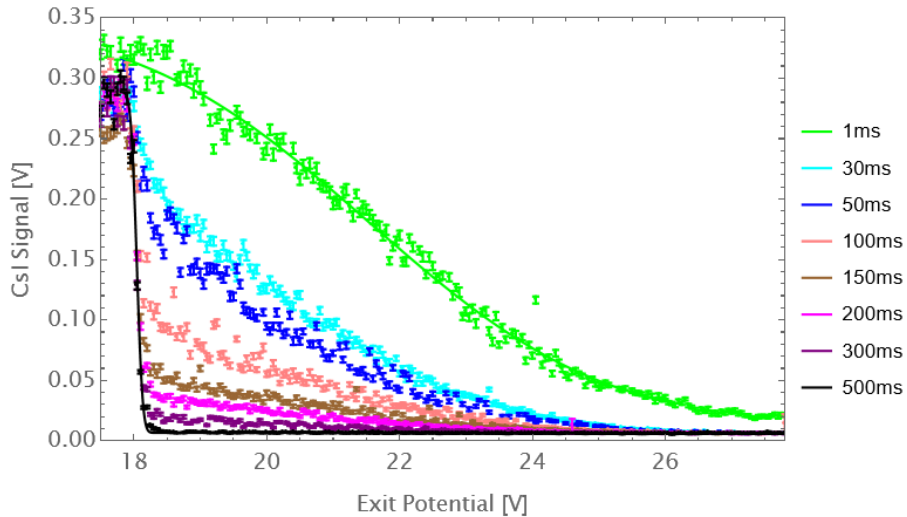
Figure 6.1: Parallel Energy measurement of a single cloud trapped in the third stage for various times. The fits are given by complementary error functions in equation 4.1. For a 1ms trap, the fitting parameters are $E_0 = (21.55 \pm 0.05)$ eV and $\sigma = (2.741 \pm 0.058)$ eV. For a 500 ms trap the fitting parameters $E_0 = (18.044 \pm 0.002)$ eV and $\sigma = (0.0692 \pm 0.003)$ eV.

Figure 6.1 shows the parallel energy measurement is taken for various trapped times. In the third stage, the last electrode is lowered in small incremented voltages allowing only particles with sufficient energy to be detected, similar to the

energy measurements previously taken in the two-stage accumulator. The cooling time is inversely proportional to the pressure in the trap and it is assumed that there is only the cooling gas, Sulfur hexafluoride, present. For 1ms and 500ms, the data is assumed to be Gaussian and can be fitted fairly with a complementary error function given by equation 4.1. The fits are visible in figure 6.1. By inspection, it is possible there are multiple distributions present.

6.2 Stacking of Two Clouds

Only single clouds of positrons have been investigated thus far. When one cloud of positrons is accumulated and transferred, this is called a stack. The accumulation and transfer process can be repeated to produce a number of stacks in the third stage. Any losses that occur prior to transfer in the preparation steps (magnetron kick) are disregarded when considering a transfer efficiency in this chapter. The signal from the stacking procedure for a single cloud and then two clouds was measured at 2 Hz accumulation.
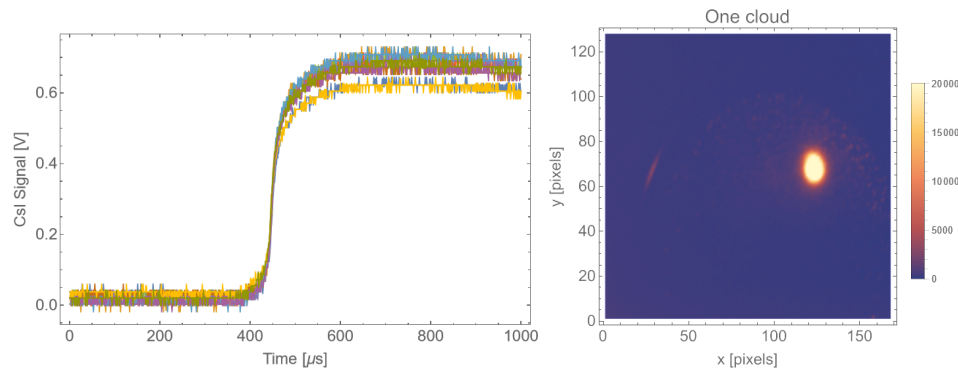
Figure 6.2: The CsI signal and MCP image of a single cloud transferred on axis and trapped. The signal is given by the mean and standard error of 10 measurements as (0.674 ± 0.013) V.
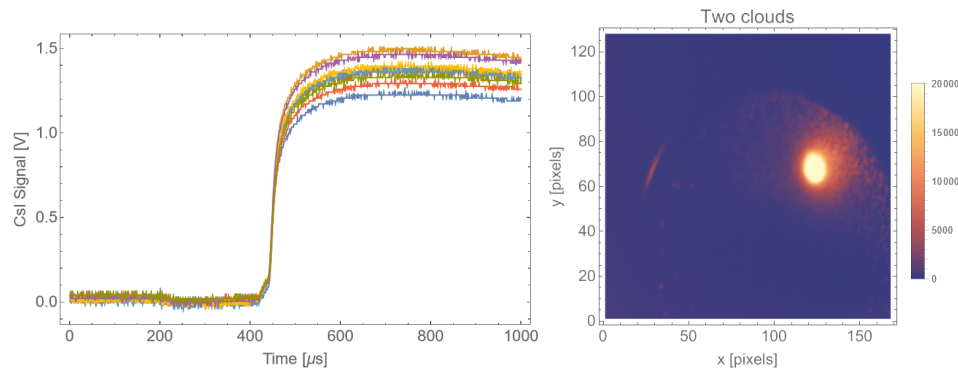
Figure 6.3: The CsI signal and MCP image of two clouds stacked. The signal is given by the mean and standard error of 10 measurements as (1.36 ± 0.02) V.

The measurements in figures 6.2 and 6.3 show that within the uncertainties, the number of positrons detected after two clouds is double that of the single cloud, which is the best outcome for stacking. The absence of any charge loss resulting in a signal less than double is due to a multitude of factors, some of which previously described in this study, such as the on axis transfer and the potential well. Also, the absence of any signal detection on the second CsI detector, placed at X2, indicates no positrons are coming out 'backwards' i.e. towards the source, indicating further that the positrons are thermalised in the well and sufficiently trapped after the second accumulation time of 500 ms.

6.3   Parallel Energy Measurement of Two Clouds

The parallel energy of the two clouds was measured by the same process as for a single cloud. The result is shown in figure 6.4. The fit parameters E_0 and σ extracted from the complimentary error functions yield information about the mean energy and energy spread. Recalling the same data from figure 6.1, the mean energy after 500 ms is seen to be slightly greater with two clouds, indicating the addition of the second cloud caused slight heating, which is not unreasonable. The energy spread is also comparable.
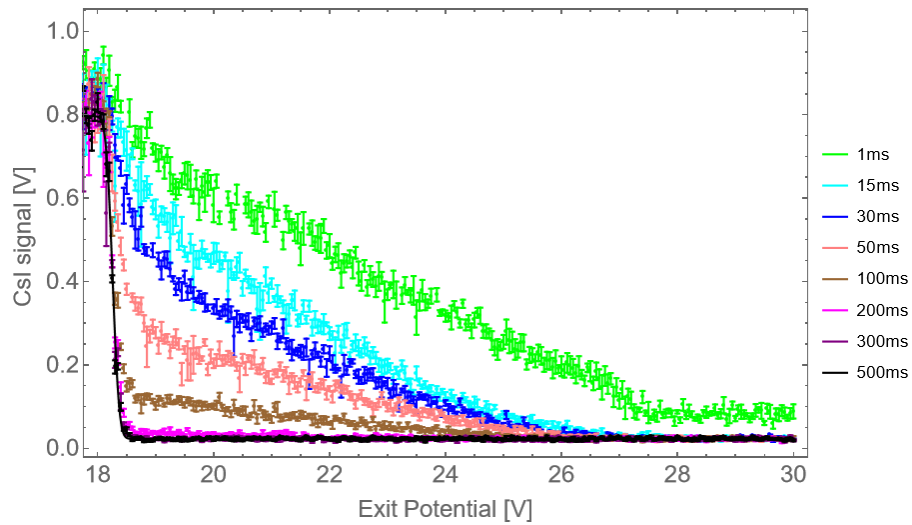
Figure 6.4: The parallel energy of two clouds, transferred on axis, with various cooling time holds. The data for 500 ms is fitted with a complementary error functions in equation 4.1. The fitting parameters $E_0 = (18.257 \pm 0.002)$ eV and $\sigma = (0.087 \pm 0.003)$ eV.

6.4   Lifetime Measurements of Two Clouds

The number of positrons and the lifetime was measured as a function of the injection position of a second cloud, where this second cloud has its position offset through uses of magnetron orbit excitation, while there exists a cloud on axis in the trap. This is measured with respect to the center of the (third stage) trap. The number of positrons that are detected is unchanged when the radial injection position of the second cloud is altered, therefore the process of injecting a second cloud does not directly lead to any looses, within the measurable uncertainties. Figure 6.5 shows that the influence of the second cloud's position is negligible on the lifetime.
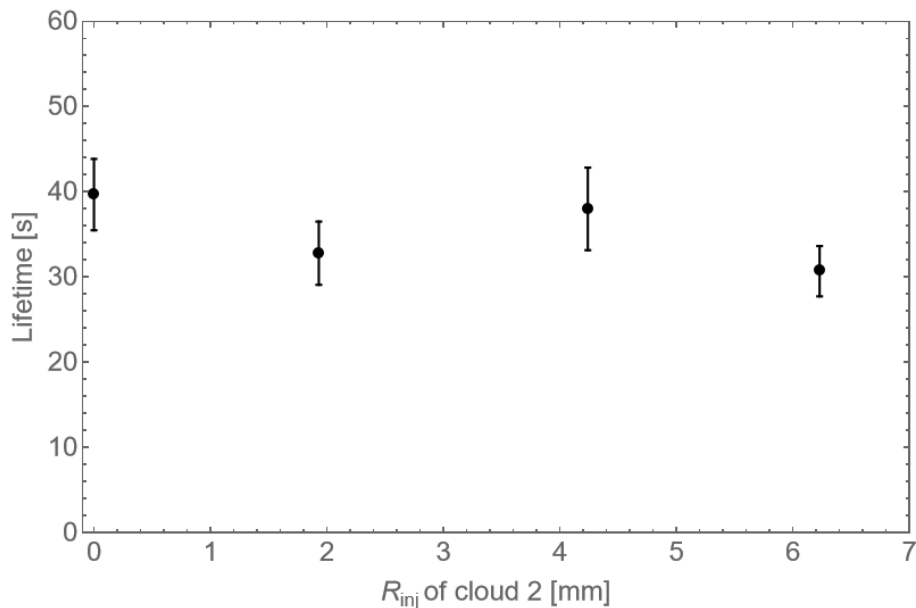
Figure 6.5: The lifetime of two clouds for varied injection positions. The data points are the mean and standard error of 3 separate lifetime measurements.

6.5   Cloud Expansion

The expansion rate of two clouds is measured by fitting a two dimensional Gaussian fit in equation 5.1 to images taken for hold times up to one second. The result is shown in figure 6.6. There is an expansion rate observed supports the long lifetime in the trap. In comparison to the single cloud expansion in figure 5.6, there is only a single expansion rate for two clouds. This leads to the assumption that the slow expansion rate observed for two clouds on axis is dominated by the first cloud that already exists on axis in the trap. This also means one can assume that the fast expansion rate that occurs at times < 150 ms in the figure 5.6 is only due to catching of positrons when there is nothing in the trap.
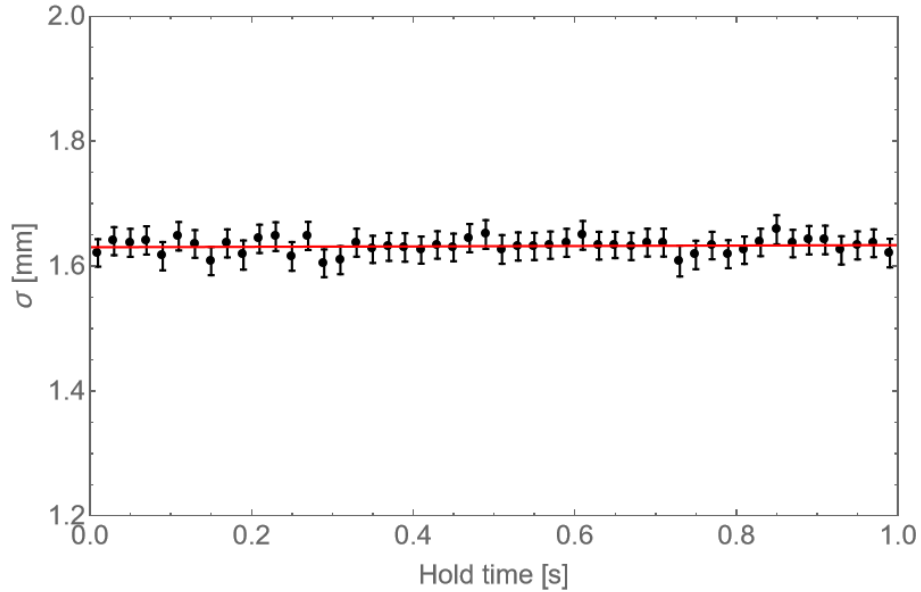
Figure 6.6: A measure of the cloud width for hold times up to 1s. The linear fit line (red) yields an expansion rate of (0.0033 ± 0.0059) mm s^{-1}.

6.6 Positron Cloud Stacking

The on axis method for stacking two clouds (which leads to double the number of positrons) is repeated for stacks > 2. The result is shown in figure 6.7, where there is a linear relationship between the number of positrons and the number of stacks transferred. Each transfer in this data set is near 100 % transfer efficiency.

If more than 7 stacks were accumulated with the current setup, at some point the relationship will not be linear and saturate at a certain number of positrons. This is due to the space charge effects in the potential well and therefore the well would need to be deepen with each transfer. The detectors would also reach a value where they would saturate, in which case a calibration would be needed where one detector is placed at a further physical location from the positron annihilations.

Once large numbers of positrons are trapped in the third stage, an enhancement in the lifetime can be made through the use of double rotating wall compression [30].
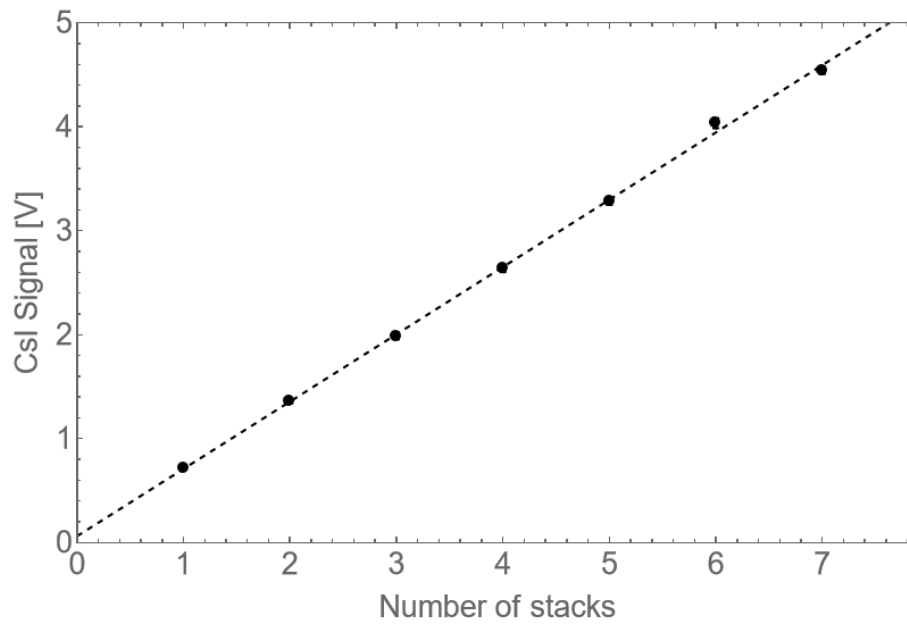
Figure 6.7: Stacking plot of 7 clouds. Each data point is the mean and standard error of 20 measurements. The dashed line is a linear fit.

Chapter 7

Final Remarks

7.1 Discussions and Conclusions

This work has produced close to 100 % transfer efficiency as shown in figure 4.12. Measurements of the parallel energy of the incoming cloud are essential to approximate the receiving well to the cloud, that is necessary for an optimised catch. The parallel energy of the cloud was measured where the potential was lowered on the electrode. A 1 ms cooling wait was added, and the measured mean energy was given as at (28.434 ± 0.003) eV with a FWHM of (0.096 ± 0.009) eV, as shown in figure 4.4. For transfer, a fast high voltage pulse generator was used as a gate to eject the particles from the two-stage accumulator, and in doing so the energy spread was increased substantially: the measured mean energy was given as (25.10 ± 0.02) eV with a FWHM of (3.13 ± 0.04) eV, as shown in figure 4.5. A simulation of the parallel energy of particles was run on SIMION, which was in fair agreement with the experimental data, with the fast gated ejection, as shown in figure 4.6. An increased axial potential in the trap reduces the particle's kinetic energy, therefore resulting in control of the particle's velocity, as shown in figures 4.9 and 4.10.

It has been shown that aligned traps (or an on axis transfer procedure) are necessary for longer lifetimes, with an on axis lifetime of 43 s observed, that decreases to 14 s when off axis, as shown in figure 5.10. The method to overcome trap misalignment (due to the movement of solenoid 3) by exciting the magnetron orbits of the particles produced a halo, which led to a recapture efficiency of 60-70 % of positrons prior to ejection and transfer. The cloud widths as a function of the injection positron were measured whilst trapped in the third stage. The expansion rate of the trapped cloud, on axis, was seen to have two components, shown in figure 5.6; a rapid expansion at times $0 < t < 100$ ms was given as (1.08 ± 0.10) mm s^{-1} and a second slow expansion rate for times $100 < t < 1000$ ms is given as (0.033 ± 0.006) mm s^{-1}. The off axis cloud widths were seen to increase rapidly at short times, and saturate at a final cloud width which was much greater than the width after 500 ms observed on axis, shown in figure 5.8. A process called

stacking was performed where clouds are accumulated and stored together in the third stage. A linear relationship was found during stacking, of the number of positrons detected with the number of stacks. The linear relationship was observed up to seven stacks, which is shown in figure 6.7.

The stacking procedure can be done with a number of clouds greater than seven and is anticipated to show a linear relationship. There are two CsI detectors available, so one detector can be placed at a further physical distance from the area of annihilation detection, and the number of particles can be calibrated through use of the 'r squared' law assuming a point source. The number of particles in the potential well at some point will exceed the space charge, and therefore the anticipated relationship would saturate. To overcome this, the well would need to deepen with the number of transfers, as performed by the GBAR collaboration [9]. If the well would be too deep to begin with, there would be an adverse effect on the lifetime.

Obtaining a greater understanding of the transfer efficiency and the interactions between stacked clouds will improve the availability of rare antimatter particles in large numbers. This is useful for antihydrogen experiments at CERN such as GBAR [9], ALPHA [8] and ASACUSA [10]. The transfer procedure is essential to make most of the experiments successful since positrons (or other charged particles) are often needed in different type of particle trap, such as cryogenic, high magnetic field or ultra high vacuum. The GBAR collaboration want to maximise the number of positrons for the production of antihydrogen ions, therefore 100% efficiency would be desirable.

7.2 Further Work

A 100% efficiency can be achieved consistently with further work built upon factors mentioned in this thesis. Trap alignment has been shown to be crucial, therefore time needs to be taken to improve the alignment of solenoids 2 and 3. This would surpass the need for the magnetron kick technique to be used, however could be used in further studies for off axis injection of particles or repositioning the cloud. The fast pulser which lowers the gated potential is used throughout, and is shown to increase the energy spread by a factor of 28. The transfer is possible without the use of fast gates, however time restrictions surpassed the need to use a slow transfer procedure. Systematic studies of the potential well could be performed in the third stage to better improve the stacking efficiency, such as a double well (one for catching the new ejection and a second to mix with existing stacks) or deepening the well with each stack [9]. An increase in positron lifetime in the third stage can be achieved, however it is highly dependant on the background gas pressure. Due to bringing the system up to atmospheric pressure on multiple occasions (due to scheduled power maintenance) the vacuum quality was variable throughout. Use of the double rotating wall in the third stage such

as performed by Evans [30] will increase the lifetime of particles to greater than 60 s.

The fundamental laws of physics can be directly tested by probing the properties of positronium (Ps), the electron positron bound state. Experiments to investigate the properties of Ps involve the excitation of Rydberg positronium [37] and gravitational free-fall measurements [38] (not exhaustive). Positronium experiments can be performed on the Swansea system, which requires positron accumulation and transfer of particles into the third stage before Ps formation.

Bibliography

1. Charlton, M. & Humberston, J. W. *Positron Physics* (Cambridge University Press, 2000).

2. Oppenheimer, J. R. Note on the Theory of the Interaction of Field and Matter. *Phys. Rev.* **35,** 461–477 (5 Mar. 1930).

3. Dirac, P. Quantised Singularities in the Electromagnetic Field (May 1931).

4. Anderson, C. D. The Positive Electron. *Phys. Rev.* **43,** 491 (6 Mar. 1933).

5. Joliot, F. & Curie, I. Artificial Production of a New Kind of Radio-Element. *Nature* **133,** 201–202 (1934).

6. Murphy, T. J. & Surko, C. M. Positron trapping in an electrostatic well by inelastic collisions with nitrogen molecules. *Phys. Rev. A* **46,** 5696–5705 (9 Nov. 1992).

7. Surko, C. M., Leventhal, M. & Passner, A. Positron Plasma in the Laboratory. *Phys. Rev. Lett.* **62,** 901–904 (8 Feb. 1989).

8. Amole, C. *et al.* The ALPHA antihydrogen trapping apparatus. *Nuclear Instruments and Methods in Physics Research Section A: Accelerators, Spectrometers, Detectors and Associated Equipment* **735,** 319–340 (2014).

9. Blumer, P. *et al.* Positron accumulation in the GBAR experiment. *Nuclear Instruments and Methods in Physics Research Section A: Accelerators, Spectrometers, Detectors and Associated Equipment* **1040,** 167–263 (2022).

10. Kuroa, N. *et al.* A source of antihydrogen for in-flight hyperfine spectroscopy. *Nature Communications* **5,** 3089 (2014).

11. Aghion, S. *et al.* Positron bunching and electrostatic transport system for the production and emission of dense positronium clouds into vacuum. *Nuclear Instruments and Methods in Physics Research Section B: Beam Interactions with Materials and Atoms* **362,** 86–92 (2015).

12. Comeau, D. *et al.* Efficient transfer of positrons from a buffer-gas-cooled accumulator into an orthogonally oriented superconducting solenoid for antihydrogen studies. *New Journal of Physics* **14,** 045006 (Apr. 2012).

13. Van der Werf, D. *et al. Transfer, stacking and compression of positron plasmas under UHV conditions* in *Non-Neutral Plamsa Physics V* **692** (Dec. 2003), 172–177.

14. Charltom, M. *et al.* Positron production using a 9 MeV electron linac for the GBAR experiment. *Nuclear Instruments and Methods in Physics Research Section A: Accelerators, Spectrometers, Detectors and Associated Equipment* **985,** 164657 (January 2021).

15. Niangn, S. *Optimisation of positron accumulation in the GBAR experiment and study of space propulsion based on antimatter* PhD thesis (Paris-Saclay University, 2021).

16. Isaac, C. A. *Axialisation of Particles in a Penning-type Trap by the Application of a Rotating Dipole Electric Field and its Application to Positron Accumulation* PhD thesis (Swansea University, 2010).

17. Vehanen, A., Lynn, K., Schultz, P. & Eldrup, M. Improved Slow-Positron Yield using a Single Crystal Tungsten Moderator. *Applied Physics A: Materials Science Processing* **32,** 163–167 (1983).

18. Gullikson, E. M. & Mills, A. P. Positron Dynamics in Rare-Gas Solids. *Phys. Rev. Lett.* **57,** 376–379 (3 July 1986).

19. Mills, A. P., Jr. and Gullikson, E. M. Solid neon moderator for producing slow positrons. *Applied Physics Letters* **49,** 1121–1123 (Oct. 1986).

20. Schultz, P. J. & Lynn, K. G. Interaction of positron beams with surfaces, thin films, and interfaces. *Rev. Mod. Phys.* **60,** 701–779 (3 July 1988).

21. Penning, F. Die glimmentladung bei niedrigem druck zwischen koaxialen zylindern in einem axialen magnetfeld. *Physica* **3,** 873–894 (9 1936).

22. Dehmelt, H. Radiofrequency Spectroscopy of Stored Ions I: Storage. *Advances in Atomic and Molecular Physics* **617,** 53–72 (1968).

23. Dehmelt, H. Radiofrequency Spectroscopy of Stored Ionss II: Spectroscopy. *Advances in Atomic and Molecular Physics* **5,** 109–154 (1969).

24. Greaves, R. & Surko, C. Positron trapping and the creation of high-quality trap-based positron beams. *Nuclear Instruments and Methods in Physics Research Section B: Beam Interactions with Materials and Atoms* **192,** 90–96 (2002).

25. Leite, A. M. M. *Development of a buffer gas trap for the confinement of positrons and study of positronium production in the GBAR experiment* PhD thesis (Université Paris-Saclay, 2017).

26. Greaves, R. & Surko, C. Radial Compression and inward transport of positron plasma using a rotating electric field. *Phys. Plasmas* **8,** 1879 (2001).

27. Baker, C. J. *Studies of magnetized positronium and of positron dynamics in a rotating dipolar electric field* PhD thesis (Swansea University, 2009).

28. Clarke, J., van der Werf, D. P. & Griffiths, B. Design and operation of a two-stage positron accumulator. *Review of scientific instruments* **77,** 063302 (2006).

29. Mortensen, T. *Manipulation of the magnetron orbits of particles and clouds in a two-stage buffer gas accumulator* PhD thesis (Swansea University, 2013).

30. Evans, H. T. *Double Rotating Wall Compression of Positron Clouds and Towards Resistive Cooling* PhD thesis (Swansea University, 2022).

31. Iwata, K., Greaves, R. G., Murphy, T. J., Tinkle, M. D. & Surko, C. M. Measurements of positron-annihilation rates on molecules. *Phys. Rev. A* **51,** 473–487 (1 Jan. 1995).

32. Van der Werf, D. P. *et al.* The behaviour of positron clouds in the single-particle regime under the influence of rotating wall electric fields. *New Journal of Physics* **14,** 075022 (2012).

33. Deller, A., Mortensen, T., Isaac, C. A., van der Werf, D. P. & Charlton, M. Radially selective inward transport of positrons in a Penning–Malmberg trap. *New Journal of Physics* **16,** 073028 (July 2014).

34. Eggleston, D. L., Driscoll, C. F., Beck, B. R., Hyatt, A. W. & Malmberg, J. H. Parallel energy analyzer for pure electron plasma devices. *Physics of Fluids B: Plasma Physics* **4,** 3432–3439 (1992).

35. Manura, D. J. & Dahl, D. A. *SIMION Version 8.0 User Manual* (Scientific Instrument Services, INC., 2006).

36. Mortensen, T. *et al.* Manipulation of the magnetron orbit of a positron cloud in a Penning trap. *Physics of Plasmas* **20.** 012124 (Jan. 2013).

37. Baker, C. *et al.* Excitation of positronium: From the ground state to Rydberg levels. *Journal of Physics B: Atomic, Molecular and Optical Physics* **51,** 035006 (Feb. 2018).

38. Cassidy, D. B. & Hogan, S. D. Atom control and gravity measurements using Rydberg positronium. *International Journal of Modern Physics: Conference Series* **30,** 1460259 (2014).